# 2D characterization of near-surface V P/V S: surface-wave dispersion inversion versus refraction tomography

Sylvain Pasquet, Ludovic Bodet, Laurent Longuevergne, Amine Dhemaied, Christian Camerlynck, Fayçal Rejiba, Roger Guérin

▶ **To cite this version:**

Sylvain Pasquet, Ludovic Bodet, Laurent Longuevergne, Amine Dhemaied, Christian Camerlynck, et al.. 2D characterization of near-surface V P/V S: surface-wave dispersion inversion versus refraction tomography. Near Surface Geophysics, 2015, 13 (4), pp.315-331. 10.3997/1873-0604.2015028 . hal-01187714

**HAL Id: hal-01187714**

**https://hal.sorbonne-universite.fr/hal-01187714**

Submitted on 27 Aug 2015

**HAL** is a multi-disciplinary open access archive for the deposit and dissemination of scientific research documents, whether they are published or not. The documents may come from teaching and research institutions in France or abroad, or from public or private research centers.

L'archive ouverte pluridisciplinaire **HAL**, est destinée au dépôt et à la diffusion de documents scientifiques de niveau recherche, publiés ou non, émanant des établissements d'enseignement et de recherche français ou étrangers, des laboratoires publics ou privés.

# 2D characterization of near-surface $V_P/V_S$: surface-wave profiling *versus* refraction tomography

Sylvain Pasquet[a,*], Ludovic Bodet[a], Laurent Longuevergne[b], Amine Dhemaied[c], Christian Camerlynck[a], Fayçal Rejiba[a], Roger Guérin[a]

[a] *Sorbonne Universités, UPMC Univ Paris 06, CNRS, EPHE, UMR 7619 METIS, 4 place Jussieu, 75005 Paris, France*
[b] *Université Rennes I, CNRS, UMR 6118, Géosciences Rennes, 35042 Rennes, France*
[c] *École des Ponts ParisTech, UMR 8205, CERMES, 77420 Champs-sur-Marne, France*

**Abstract**

The joint study of pressure (P-) and shear (S-) wave velocities ($V_P$ and $V_S$), as well as their ratio ($V_P/V_S$), has been used for many years at large scales but remains marginal in near-surface applications. For these applications, $V_P$ and $V_S$ are generally retrieved with seismic refraction tomography combining P and SH (shear-horizontal) waves, thus requiring two separate acquisitions. Surface-wave prospecting methods are proposed here as an alternative to SH-wave tomography in order to retrieve pseudo-2D $V_S$ sections from typical P-wave shot gathers and assess the applicability of combined P-wave refraction tomography and surface-wave dispersion analysis to estimate $V_P/V_S$ ratio. We carried out a simultaneous P- and surface-wave survey on a well-characterized granite–micaschists contact at Plœmeur hydrological observatory (France), supplemented with an SH-wave acquisition along the same line in order to compare $V_S$ results obtained from SH-wave refraction tomography and surface-wave profiling. Travel-time tomography was performed with P- and SH-wave first arrivals observed along the line to retrieve $V_P^{tomo}$ and $V_S^{tomo}$ models. Windowing and stacking techniques were then used to extract evenly spaced dispersion data from P-wave shot gathers along the line. Successive one-dimensional Monte Carlo inversions of these dispersion data were performed using fixed $V_P$ values extracted from the $V_P^{tomo}$ model and no lateral constraints between two adjacent one-dimensional inversions. The resulting one-dimensional $V_S^{sw}$ models were then assembled to create a pseudo-2D $V_S^{sw}$ section, which appears to be correctly matching the general features observed on the $V_S^{tomo}$ section. If the $V_S^{sw}$ pseudo-section is characterized by strong velocity uncertainties in the deepest layers, it provides a more detailed description of the lateral variations in the shallow layers. Theoretical dispersion curves were also computed along the line with both $V_S^{tomo}$ and $V_S^{sw}$ models. While the dispersion curves computed from $V_S^{sw}$ models provide

results consistent with the coherent maxima observed on dispersion images, dispersion curves computed from $V_S^{tomo}$ models are generally not fitting the observed propagation modes at low frequency. Surface-wave analysis could therefore improve $V_S$ models both in terms of reliability and ability to describe lateral variations. Finally, we were able to compute $V_P/V_S$ sections from both $V_S^{sw}$ and $V_S^{tomo}$ models. The two sections present similar features, but the section obtained from $V_S^{sw}$ shows a higher lateral resolution and is consistent with the features observed on electrical resistivity tomography, thus validating our approach for retrieving $V_P/V_S$ ratio from combined P-wave tomography and surface-wave profiling.

*Keywords:* Seismic methods, Surface-wave profiling, P-wave tomography, SH-wave tomography, $V_P/V_S$ ratio.

---

*Corresponding author: Sorbonne Universités, UPMC Univ Paris 06, UMR 7619, METIS, case 105, 4 Place Jussieu, 75252 Paris Cedex 05, France. Phone: +33 (0)1 44 27 45 91 - Fax: +33 (0)1 44 27 45 88.

*Email address:* sylvain.pasquet@upmc.fr (Sylvain Pasquet)

## 1. INTRODUCTION

The joint study of pressure (P-) and shear (S-) wave velocities ($V_P$ and $V_S$, respectively), as well as their ratio ($V_P/V_S$), has been used for many years at large scales. $V_P/V_S$ is commonly employed in seismology and geodynamics to study oceanic and continental crusts' structures (Nicholson and Simpson 1985; Julià and Mejía 2004; Tryggvason and Linde 2006; Powell *et al.* 2014), subduction and extension zones (Nakajima *et al.* 2001; Bauer *et al.* 2003; Latorre *et al.* 2004; Gautier *et al.* 2006; Reyners *et al.* 2006), active volcanic areas (Walck 1988; Sanders *et al.* 1995; Lees and Wu 2000; Schutt and Humphreys 2004), or earthquake-source regions (Catchings 1999; Ryberg *et al.* 2012). $V_P/V_S$ has proved to be an efficient parameter to highlight the existence of melt or aqueous fluid phase (Takei 2002) since the liquid phase affects $V_P$ and $V_S$ differently (Biot 1956a,b).

Many theoretical studies (Berryman 1999; Lee 2002; Dvorkin 2008) and experimental developments (Wyllie, Gregory, and Gardner 1956; Murphy 1982; Prasad 2002; Uyanık 2011) have been aimed at understanding the effect of saturation and pore fluids on body wave velocities in consolidated media, especially in the field of hydrocarbon exploration where the $V_P/V_S$ ratio is frequently used to discriminate different pore fluids in reservoirs (Tatham and Stoffa 1976; Fu, Sullivan, and Marfurt 2006; Rojas 2008). The value of the $V_P/V_S$ ratio is also related to *in situ* stress orientation (Thompson and Evans 2000), fractures and cracks presence, and pore geometry for individual lithologies with small variations in composition (Tatham 1982; Wilkens, Simmons, and Caruso 1984).

In near-surface applications (at depth lower than 100 m), the combined study of $V_P$ and $V_S$ is often proposed without the calculation of $V_P/V_S$ ratios. It is classically carried out for engineering purposes to determine the main mechanical properties of reworked materials in active landslides (Godio, Strobbia, and De Bacco 2006; Jongmans *et al.* 2009; Socco *et al.* 2010b; Hibert *et al.* 2012), control fill compaction in civil engineering (Heitor *et al.* 2012; Cardarelli, Cercato, and De Donno 2014), study weathering and alteration of bedrock (Olona *et al.* 2010), or assess earthquake site response (Jongmans 1992; Lai and Rix 1998; Raptakis *et al.* 2000; Othman 2005). More recently, this approach has also been proposed for hydrological applications to characterize shallow aquifers (Grelle and Guadagno 2009; Mota and Monteiro Santos 2010; Konstantaki *et al.* 2013; Pasquet *et al.* 2015).

For these shallow-target studies, $V_P$ and $V_S$ are generally retrieved with seismic refraction

tomography using both P and SH (shear-horizontal) waves (Turesson 2007; Grelle and Guadagno 2009; Fabien-Ouellet and Fortier 2014; Pasquet *et al.* 2015). The use of this method is widespread since it is easily carried out with a one-dimensional (1D) to three-dimensional (3D) coverage, quick to implement and relatively inexpensive (Galibert *et al.* 2014). However, if measurements of $V_P$ are performed quite efficiently for many years, retrieving $V_S$ remains complex since it requires the use of horizontal component geophones difficult to set up horizontally (Sambuelli *et al.* 2001) and specific sources strenuous to use (Sheriff and Geldart 1995; Jongmans and Demanet 1993; Xia *et al.* 2002; Haines 2007).

As an alternative to SH-wave refraction tomography, surface-wave prospecting methods are commonly proposed to achieve indirect estimation of $V_S$ in a relatively straightforward manner (e.g., Gabriels, Snieder, and Nolet (1987); Jongmans and Demanet (1993); Park, Miller, and Xia (1999); Socco and Strobbia (2004); and Socco, Foti, and Boiero (2010a)). Due to their dispersive nature, surface waves are characterized by an investigation depth that mainly depends on the considered data frequency. Surface waves are thus widely used at large scales in global seismology for mantle investigations using low frequencies. When targeting shallow structures with strong lateral variability, surface-wave methods are, however, limited by the well-known trade-off between lateral resolution and investigation depth (Gabriels *et al.* 1987). On the one hand, the inverse problem formulation requires the investigated medium to be assumed 1D below the spread, which has to be short enough to achieve lateral resolution and perform two-dimensional (2D) profiling. On the other hand, long spreads and low-frequency geophones are required to record long wavelengths in order to increase the investigation depth and mitigate near-field effects (Russel 1987; Forbriger 2003a,b; O'Neill 2003; O'Neill and Matsuoka 2005; Bodet *et al.* 2005; Zywicki and Rix 2005; Bodet, Abraham, and Clorennec 2009). When the seismic set-up provides redundant data, several countermeasures exist to overcome these drawbacks and narrow down the lateral extent of dispersion measurements, such as common mid-point cross-correlation (Hayashi and Suzuki 2004; Grandjean and Bitri 2006; Ikeda, Tsuji, and Matsuoka 2013), multi-offset phase analysis (Strobbia and Foti 2006; Vignoli and Cassiani 2010), or offset moving windows and dispersion stacking techniques (O'Neill, Dentith, and List 2003; Bohlen *et al.* 2004; Neducza 2007; Boiero and Socco 2010, 2011; Bergamo, Boiero, and Socco 2012).

The joint analysis of travel-time tomography $V_P$ and surface-wave profiling $V_S$ has recently

been proposed to retrieve 1D time-lapse $V_P/V_S$ soundings (Pasquet *et al.* 2015) or 2D $V_P/V_S$ sections (Ivanov *et al.* 2006; Konstantaki *et al.* 2013). Pasquet *et al.* (2015) highlighted an overall consistency between the temporal variations of the water table and $V_P/V_S$ contrasts. For their part, Konstantaki *et al.* (2013) assessed the lateral fluctuations of a shallow aquifer water table level with 2D $V_P/V_S$ variations. Using a single standard acquisition set-up to retrieve 2D $V_P$ and $V_S$ sections thus appears interesting and convenient to reduce equipment costs and acquisition time. Yet, refraction tomography and surface-wave profiling involve distinct characteristics of the wavefield and different assumptions about the medium, thus providing results of different resolutions and investigation depths difficult to compare to each other.

This study tackles such issues through a systematic comparison of $V_S$ models obtained from SH-wave refraction and surface-wave dispersion inversion, along with $V_P$ retrieved from P-wave refraction, as recently proposed by Pasquet *et al.* (2014, 2015). For this purpose, we targeted the Plœmeur hydrological observatory (France). This experimental site has been subject to many geophysical and hydrogeological studies aimed at characterizing the flow processes involved in the recharge of the outstandingly productive fractured aquifer present in the region (Touchard 1999; Le Borgne *et al.* 2006a,b, 2007; Ruelleu *et al.* 2010; Jiménez-Martínez *et al.* 2013). The study area is located at a contact between granites and micaschists, clearly highlighted in the surface by electrical resistivity tomography (ERT) and electrical conductivity (EC) mapping. However, previous refraction seismic studies showed that $V_P$ alone was neither able to detect the contact zone nor able to discriminate granites from micaschists, probably because P-wave velocity is mainly controlled by the water content in the weathered areas. The site consequently provided a challenging framework to test the applicability of the joint interpretation of $V_P$ and $V_S$ for near-surface applications. In the present study, $V_P$ and $V_S$ sections were classically obtained with P- and SH-wave travel-time tomography carried out on a line intersecting the contact zone. Surface-wave profiling was performed by means of offset moving window and dispersion stacking techniques. Local dispersion measurements were first extracted from different shots illuminating the same portion of the seismic line and then stacked to increase signal-to-noise ratio. The extraction window was eventually moved along the line to retrieve a collection of local multimodal dispersion measurements. Several window lengths were tested to find the best compromise between lateral resolution and investigation depth (Pasquet *et al.* 2012). The lateral consistency of dispersion data was thoroughly controlled during

picking through visual browsing and *a posteriori* verified on phase velocity pseudo-sections. Separate Monte Carlo inversions of dispersion curves were then performed along the line with no lateral constraints in order to reconstruct a pseudo-2D $V_S$ section. The parameterization of those inversions was based on: (i) $V_P$ obtained from travel-time tomography; (ii) *a priori* geological knowledge; and (iii) maximum wavelengths observed along the line. Theoretical dispersion curves were then recomputed from both $V_S$ models along the line to control the inversion quality and the consistency of these models. Finally, $V_P/V_S$ obtained from both methods were compared to evaluate their ability to image $V_P/V_S$ variations and assess their practical limitations.

## 2. SITE DESCRIPTION AND DATA ACQUISITION

### *2.1. Geological setting*

The Plœmeur site is located on the south coast of Brittany (west of France), 3 km far from the Atlantic Ocean, near the city of Lorient (Fig. 1). The crystalline bedrock aquifer present in the area is composed of tectonic units developed during the Hercynian orogeny and marked by numerous synkinematic intrusions of upper Carboniferous leucogranites (Ruelleu *et al.* 2010). The pumping site is located at the intersection of: (i) a contact between the Plœmeur granite and overlying "Pouldu" micaschists dipping 30° to the North and (ii) a subvertical fault zone striking N 20° (Fig. 1). Weathering in the area is limited to the first few metres, except in the micaschists near the pumping site where it reaches about 30 m. Before the start of the pumping activities in 1991, the site was a natural aquifer discharge area with preferential upward fluxes. The average water levels began to decline during the first years of operation but have stabilized since 1997 (Jiménez-Martínez *et al.* 2013). Despite the low permeability and porosity of these lithologies, pumping wells implanted in the site have been continuously producing water at a rate of about $10^6$ $m^3$ per year since 1991 (Touchard 1999), with limited head decrease and no seawater intrusion. One of the challenges on this site is to understand recharge processes in these highly heterogeneous systems. For this purpose, the site is monitored by several wells implanted mostly around the contact zone and in the clayey area overlaying micaschists (F* and MF* in Fig. 2).

### *2.2. Previous geophysical results*

Slingram EC mapping and ERT were carried out on the site prior to the seismic campaign in order to accurately describe near-surface lithologies. Apparent EC ($\sigma_a$) variations over the first

5.5 m in depth were mapped using an electromagnetic device with low induction number (intercoil spacing of 3.66 m and frequency of 9.8 kHz) in vertical dipole (VD) configuration, integrating conductivity values down to about 6 m in depth (McNeill 1980). We used a continuous acquisition mode following profiles separated with 5 m to 7 m, covering an area of about 15 ha (Fig. 2a). As for ERT, we used a multi-channel resistivimeter with a 96-electrode Wenner–Schlumberger array and 1 roll-along (Fig. 2b). The electrodes were spaced with 4 m in order to obtain a 476-m-long profile roughly oriented west–east (WE on Fig. 2a). The inversion was performed using the RES2DINV software (Loke and Barker 1996).

Results of EC mapping show smooth lateral variations of $\sigma_a$ (from less than 5 mS/m to over 30 mS/m, i.e., from 200 Ωm to less than 30 Ωm in terms of apparent electrical resistivity $\rho_a$) in the subsurface. Western low $\sigma_a$ values are clearly associated with the presence of very shallow granite (between 0 m and 125 m along the WE profile in Fig. 2a). On the contrary, higher $\sigma_a$ values observed in the eastern part can be related to clays overlaying weathered micaschists (between 275 m and 476 m in Fig. 2a). Such distribution seems in agreement with the assumption of the contact zone striking N 20° in the area. ERT results are also consistent with the anticipated geological structures in depth and clearly match the apparent EC variations in surface (Fig. 2b). Four main structures can be delineated in Fig. 2b: fresh granite (FG), almost outcropping in the western part, characterized by high-electrical-resistivity ($\rho$) values (around 1000 Ωm); weathered granite (WG), at the surface in the western part, characterized by significantly lower $\rho$ values (around 200 Ωm); clays (CL), at the surface in the eastern part, characterized by slightly lower $\rho$ values (between 50 Ωm and 200 Ωm); and micaschists (MS), deeper in the eastern part, characterized by higher $\rho$ values (around 750 Ωm). Possible evidence of the contact zone is visible between 225 m and 250 m along the ERT profile, marking a strong contrast between WG and clays (hashed area in Fig. 2b). The positions of the nearest piezometric wells are projected on the WE line with their measured piezometric head level. A significant decrease in this level is observed in the wells located in the hashed area due to pumping occurring in the F28 well. While Pasquet *et al.* (2015) studied $V_P/V_S$ in simplified 1D conditions, this site offers the perfect framework to address 2D issues (i.e., presence of strong lateral variations of lithology and topography), especially when knowing that previous P-wave tomography studies failed to depict these lateral variations.

### *2.3. Seismic acquisition*

The seismic acquisition set-up was deployed along the ERT profile (WE in Fig. 2a). It consisted of a simultaneous P- and surface-wave acquisition followed by an SH-wave acquisition along the same line. We used 72 geophones, a 4-m receiver spacing and 2 roll-alongs to finally obtain a 476-m-long profile (Fig. 3). A 72-channel seismic recorder was used with 14-Hz vertical component geophones for the P-wave and surface-wave profiles and with 14-Hz horizontal component geophones for the SH-wave profile. The use of 14-Hz geophones offers a good compromise to obtain seismic records with a frequency content suitable for surface-wave, refraction, and reflection processing. First shot location was one-half receiver spacing away from the first trace, and move-up between shots was one receiver interval in order to achieve the high coverage required to perform refraction tomography and to stack dispersion data. In addition, 219 shots were recorded along each profile for a total number of 15768 active traces. The P-wave source consisted of an aluminium plate hit vertically by a 5-kg sledgehammer. The plate was hit six times at each position to increase signal-to-noise ratio. SH waves were generated with a handheld source consisting of a heavy metal frame hit laterally by a 5-kg sledgehammer. The SH-wave source was hit 12 times at each position. For both P- and SH-wave acquisitions, the sampling rate was 0.25 ms and the recording time was 2 seconds to include full surface-wave wavefield. A delay of $-0.02$ seconds was kept before the beginning of each record to prevent early triggering issues. The collected data presented on Fig. 4 are affected with a significant noise level, especially at far offset (80 m and more), due to active pumping wells and military airplanes regularly landing and taking off from a nearby air force base. Seismograms clearly show lateral variations due to both topographic effects and subsurface velocity changes, with strong attenuation over clays and micaschists in the eastern part of the line.

## 3. TRAVEL-TIME TOMOGRAPHY

### *3.1. Travel-time data*

We applied DC removal and a zero-phase low-pass filter on both P- and SH-wave data to remove high-frequency noise (>100 Hz) and help for first arrival identification at far offsets. For the P-wave profile, a total of 7076 first arrivals (45% of all traces) were determined (Fig. 5a) and 10352 traces (65% of all traces) were picked on SH-wave shots (Fig. 5c). Travel-time data could not be obtained where noise level was too high (grey dots in Fig. 5), with average maximum offsets around 100 m

for P waves and around 150 m for SH waves. Travel times are represented in a source–receiver diagram (Fig. 5), which shows the distribution of first arrival times for each source–receiver pair (Bauer *et al.* 2010; Baumann-Wilke *et al.* 2012). The diagonal traces indicate the zero-offset travel times, where source and receiver locations are identical. This representation gives a first impression of the subsurface velocity structure and allows for checking the lateral consistency of picked travel times. Three main areas are clearly visible on both P- and SH-wave first arrivals: the first area (from 0 m to 125 m) is characterized by the shortest first arrival times (i.e., shallow high velocity zone); the area between 125 m and 275 m depicts slightly increasing times; and the third area (from 275 m up to the end of the line) shows greater arrival times (compared with the first area), probably associated with shallow low velocities.

The distribution depicted in Fig. 5a and 5c appears interestingly related to the lateral variability observed on the EC map (Fig. 2a). Along the seismic profile, very low $\sigma_a$ values occur between 0 m and 125 m on the granite side and are coherent with short first arrival times. High-$\sigma_a$ values observed between 275 m and the end of the line are also consistent with the shallow low velocity zone suggested by long first arrival times. In the centre part (from 125 m to 275 m), intermediate apparent EC values are in agreement with slightly decreasing shallow velocities observed in Fig. 5a and 5c, suggesting a thickening of the weathered layer.

### *3.2. Tomography inversion*

Travel-time data were inverted with the refraction tomography software RAYFRACT (Schuster and Quintus-Bosz 1993; Sheehan, Doll, and Mandell 2005; Rohdewald 2011) using a smooth gradient initial model. This model is the 2D extension of the mean 1D model obtained directly from picked travel times, assuming velocity gradients in a 1D tabular medium (Gibson, Odegard, and Sutton 1979). It varied from 10 m/s at the surface to 3500 m/s at 40 m in depth for the P-wave model and from 10 m/s at the surface to 2000 m/s at 40 m in depth for the SH-wave model. The inversion process was stopped when velocity update, global root-mean-square (RMS) error, and maximum normalized residual reached minimum values. In addition, 30 iterations were needed for both P- and SH-wave travel times. For the P-wave profile, the global RMS error (in blue in Fig. 6b) and the maximum normalized residual (in red in Fig. 6b) both steeply decrease during the first six iterations, i.e., from 5 ms to 2.5 ms and from 25 ms to 13 ms, respectively, and more gradually during the last iteration steps until they both reach minimum values of 2.1 ms and 11.5 ms, respectively. Mean

velocity update also rapidly decreases to reach a minimum value after six iterations (in black in Fig. 6c). Maximum and minimum velocity updates (in red and blue, respectively, in Fig. 6c) are more perturbated and tend to stabilize only after 20 iterations. As for SH-wave data, the global RMS error (in blue in Fig. 6e) and the maximum normalized residual (in red in Fig. 6e) both quickly decrease during the first 10 iterations, i.e., from 12.5 ms to 6 ms and from 50 ms to 22 ms, respectively, and more smoothly during the last iteration steps until they both reach minimum values of 4.3 ms and 20.1 ms, respectively. Mean, maximum, and minimum velocity updates (in black, red, and blue, respectively, in Fig. 6f) reach minimum values after 10 iterations.

Normalized residuals were computed between observed and calculated travel times for every picked trace (Bauer *et al.* 2010). Their distributions are represented in source–receiver diagrams for both P- (Fig. 5b) and SH-wave (Fig. 5d) travel times. P-wave inversion results have lower global RMS values (2.1 ms for P waves; 4.3 ms for SH waves) and maximum residual values (11.5 ms for P waves; 20.1 ms for SH waves), and the mean residual value is higher for P waves (6.7%) than for SH waves (3.9%). The ratio of residuals below 10% is also higher for SH-wave models (around 93%) than for P-wave models (around 91%). The distribution of residuals shows the highest values at near offsets, probably due to shallow lateral heterogeneities and triggering issues during the acquisition.

The final velocity models were clipped for both $V_P$ (Fig. 6a) and $V_S$ (Fig. 6d) sections below a ray coverage of 100 rays per grid cell to keep only well-resolved areas. Both models are characterized by velocities mainly following a linearly increasing trend in depth and show no strong lateral variations. Only slight perturbations of the initial gradient model along the line can be observed with: (i) higher $V_P$ and $V_S$ in the western part ($HV_P$ and $HV_S$, respectively), corresponding to the high-electrical-resistivity values associated with FG; (ii) lower $V_P$ in the centre ($LV_P$), consistent with a decrease in the piezometric head level and evidences of the contact zone inferred from ERT; and (iii) lower $V_S$ in the eastern part of the profile ($LV_S$).

## 4. SURFACE-WAVE PROFILING

### *4.1. Extraction of dispersion curves*

Our multifold acquisition set-up allowed us to obtain surface-wave dispersion images from P-wave shot gathers using windowing and dispersion stacking to narrow down the lateral extent of dispersion measurements and increase the signal-to-noise ratio. Dispersion stacking was performed

following the basic workflow derived from O'Neill *et al.* (2003).

1. Select $nW$ traces centred on a specific position along the line ($Xmid$).
2. Load a shot illuminating the selected spread.
3. Window the $nW$ traces in the selected shot record.
4. Transform the wavefield to the frequency-phase velocity domain (dispersion image).
5. Normalize amplitude spectrum at each frequency.
6. Repeat steps 2–5 for the $nS$ selected shots.
7. Stack all normalized dispersion images and pick the dispersion curves for each identified propagation mode from the final image.
8. Shift the window of $dW$ traces to the next $Xmid$ and repeat steps 1–7.

As aforementioned, the difficulty is to find the best compromise between investigation depth, spectral resolution, and lateral resolution while keeping the 1D assumption valid. Thus, we first performed trial-and-error tests (Pasquet *et al.* 2012) to select the optimum window size ($nW$) and the number of sources ($nS$), keeping in mind that there is not, for the moment, any perfect criterion (Pérez Solano 2013; Pérez Solano, Donno, and Chauris 2014). A 20-m-wide window with six traces ($nW = 6$) was eventually used with six direct and six reverse shots on each side of the window ($nS = 6$). Using more sources is likely to increase signal-to-noise ratio and enhance the maxima but would narrow down the effective study area along the line (black dots in Fig. 2a). Single dispersion images were obtained from each shot using a slant stack in the frequency domain (Russel 1987; Mokhtar, Herrmann, and Russell 1988). These images (in which maxima should correspond to Rayleigh-wave propagation modes) were first compared to confirm the validity of the 1D approximation below the spread (Jongmans *et al.* 2009). These 12 single dispersion images were then stacked as a final dispersion image. The moving window was finally shifted along the line with a step of one receiver spacing ($dW = 1$, i.e., 4 m). We thus obtained evenly spaced dispersion images at each spread mid-point ($Xmid$) with a large overlap in order to retrieve smoothly varying dispersion images between two adjacent stacking windows and help for visual browsing when picking dispersion curves.

We eventually obtained a collection of 105 stacked dispersion images along the line, on which coherent maxima associated with the different propagation modes were identified. Visualization of adjacent stacked dispersion images allowed for following the progressive lateral evolution of

the different modes and for avoiding mode misinterpretation (Zhang and Chan 2003; O'Neill and Matsuoka 2005; Boaga *et al.* 2013; Ezersky *et al.* 2013). These maxima were finally extracted on each stacked dispersion image with an estimated standard error in phase velocity defined according to the workflow described in O'Neill (2003). The dispersion lateral variability is illustrated here by two examples at both sides of the line (Fig. 7a ($Xmid$ = 50 m) and 7c ($Xmid$ = 402 m)). As, for instance, recommended by Bodet (2005) and Bodet *et al.* (2009), dispersion curves were limited down to frequencies ($f_{lim}$) where the spectral amplitude of the seismogram became too low (13.5 Hz in Fig. 7b and 8 Hz in Fig. 7d). Several authors (e.g., O'Neill (2003) and Zywicki and Rix (2005)) also mentioned that wavelengths higher than 50% of the spread length should not be used in order to mitigate near-field effects and prevent from velocity underestimation at low frequency. These recommendations are only basic rules of thumb mostly valid when using the fundamental mode only. Here, we used wavelengths higher than 50% of our spread length since we were able to perform dispersion stacking and use higher modes, which are of great constraint on the inversion with a strong impact on the investigation depth (Gabriels *et al.* 1987; Xia *et al.* 2003). Furthermore, possible low-frequency discrepancies were limited by attributing important errors to dispersion data with respect to frequency and spread length (O'Neill 2003). Finally, the corresponding maximum wavelength ($\lambda_{max}$) was extracted (35 m in Fig. 7a and 37 m in Fig. 7c) to retrieve $\lambda_{max}/2$, a typical investigation depth criterion (O'Neill 2003).

Up to four propagation modes were observed along the line and identified as fundamental (0), first (1), second (2), and third (3) higher modes (only modes up to 2 were identified in the examples shown in Fig. 7). The resulting dispersion curves are presented in Rayleigh-wave phase velocity pseudo-sections as a function of the wavelength $\lambda$ and the spread mid-point $Xmid$ (Fig. 8) in order to control the lateral coherence of mode identification (Strobbia *et al.* 2011; Haney and Douma 2012; Boiero *et al.* 2013a; Ezersky *et al.* 2013). The fundamental mode pseudo-section (Fig. 8a) does not present unrealistic abrupt changes (considering the overlap between two adjacent stacking windows) but shows significant lateral variations of Rayleigh-wave phase velocities. High phase velocities (from 200 m/s to 550 m/s) exist in the western part of the line (from the beginning to around 100 m), whereas the eastern part of the line (from 275 m to the end) is characterized by lower phase velocities (around 150 m/s–200 m/s). The first (Fig. 8b), second (Fig. 8c), and third (Fig. 8d) higher modes show less lateral variations in terms of velocity, but the available frequency range for

mode 1 presents significant lateral fluctuations. The maximum wavelength ($\lambda_{max}$) observed at each $Xmid$ ranges from 20 m to 50 m with an average value around 30 m (Fig. 8e).

### *4.2. Inversion*

Assuming a 1D tabular medium below each extraction window, we performed a 1D inversion of dispersion data obtained at each $Xmid$. We used the neighbourhood algorithm (NA) developed by Sambridge (1999) and implemented for near-surface applications by Wathelet, Jongmans, and Ohrnberger (2004) and Wathelet (2008) within the GEOPSY tool (available at `www.geopsy.org`). Theoretical dispersion curves were computed from the elastic parameters using the Thomson–Haskell matrix propagator technique (Thomson 1950; Haskell 1953). NA performs a stochastic search of a pre-defined parameter space (namely, $V_P$, $V_S$, density, and thickness of each layer) using the following misfit function ($MF$):

$$MF = \sqrt{\sum_{i=1}^{N_f} \frac{(V_{cal_i} - V_{obs_i})^2}{N_f {\sigma_i}^2}} \ , \tag{1}$$

with $V_{cal_i}$ and $V_{obs_i}$ being the the calculated and observed phase velocities at each frequency $f_i$, $N_f$ being the number of frequency samples, and $\sigma_i$ being the phase velocity measurement error at each frequency $f_i$.

An appropriate choice of these parameters is considered as a fundamental issue for the successful application of inversion (Socco and Strobbia 2004; Renalier *et al.* 2010). Based on site *a priori* geological knowledge (presence of weathering gradients), we used parameterization with a stack of ten layers overlaying the half-space to look for a velocity gradient. The thickness of each layer was allowed for ranging from 0.5 m to 2.5 m. The maximum half-space depth (HSD) is of great importance since it depends on the poorly known investigation depth of the method. It was fixed to the half of the maximum wavelength observed along the entire line (25 m), as recommended by O'Neill (2003) and Bodet *et al.* (2005). The valid parameter range for sampling velocity models was 10 m/s–1500 m/s for $V_S$ (based on dispersion observations and refraction tomography), with velocities constrained to only increase with depth, based on geological *a priori* information. P-wave velocity being of weak constraint on surface-wave dispersion, only the S-wave velocity profile can be interpreted (Der and Landisman 1972; Russel 1987). However, an identical layering is required for $V_P$ and $V_S$ in order to interpret $V_P/V_S$ ratios. For this purpose, we extracted an average $V_P$ value

for each 2.5-m-thick slice of the $V_P$ model obtained from refraction tomography (Fig. 6a). This average value was then used to fix $V_P$ in each layer of the inversion parameterization. Furthermore, $V_S$ values were allowed to vary in such a way that Poisson's ratio values always remained between 0.1 and 0.5 in order to prevent from unrealistic $V_S$ values. Density was set as uniform (1800 kg/m$^3$) since its influence on dispersion curves is very limited (Der and Landisman 1972; Russel 1987). It is worth mentioning that, except for the $V_P$ values, we used the same parameterization for all the 1D inversions performed along the line. We assumed that stacking and windowing already naturally smoothed the dispersion data, thus not requiring the use of lateral constraints between successive inversions.

A total of 63000 models were generated with NA (Fig. 9a ($Xmid = 50$ m) and 9c ($Xmid = 402$ m)). Models matching the observed data within the error bars were selected, as suggested by Endrun *et al.* (2008). The accepted models were used to build a final average velocity model associated with the centre of the extraction window (dashed line in Fig. 9b ($Xmid = 50$ m) and 9d ($Xmid = 402$ m)). As the maximum HSD remains constant along the line (same parameterization for each inversion), $\lambda_{max}/2$ is given (solid black line in Fig. 9b and 9d) to show where inverted models expand below typical investigation depth criterion. Normalized residuals between observed and calculated phase velocities were computed along the line for each individual sample of the picked dispersion curves. Their distributions are represented in pseudo-sections to control the quality of the final pseudo-2D $V_S$ section. The fundamental mode residuals' pseudo-section (Fig. 10a) shows quite uniform values, with a maximum of 19%, a mean residual of 5%, and 86% of the residuals with values below 10%. Residual values obtained for the first higher mode (Fig. 10b) present higher values, especially at great wavelength. The maximum residual value is 29%, the mean is 9%, and only 62% of the residuals are below 10%. As for the second and the third higher modes (Fig. 10c and 10d, respectively), residuals remain very low with a maximum of 12% and 3%, respectively, and a mean residual of 1.8% and 1.3%, respectively. In addition, 99% of the second higher mode samples have residual values below 10%, whereas all samples of the third higher mode have residuals below 10%. We additionally computed the misfit for each 1D $V_S$ model along the line with equation (1) (Fig. 10e). Misfit values remain stable along the line and range from 0.05 to around 0.25, with a mean value of about 0.125. Several gaps are present along the line and correspond to inversions where none of the calculated models were fitting the error bars.

Each 1D $V_S$ model was then represented at its corresponding $Xmid$ position to obtain a pseudo-2D $V_S$ section (Fig. 11). All the models were represented down to the maximum HSD (25 m), with the investigation depth criterion $\lambda_{max}/2$ superimposed in hashed black line. With such a representation, the actual HSD of each model can be easily followed along the line and compared with the investigation depth criterion. If the lateral variations of $V_S$ values remain remarkably smooth in the shallow layers, the deepest layers and the half-space present an important variability of $V_S$ caused by the higher uncertainties in dispersion measurements at great wavelength (i.e., higher residual values in Fig. 10). Global results show a shallow low velocity layer ($\sim$ 250 m/s), which is thinner in the western part of the line (from 3 m to 6 m) and becomes thicker ($\sim$ 10 m) in the eastern part. High velocities (between 500 m/s and 1000 m/s) can be observed in the western part, directly below the shallow low velocity layer, whereas the velocity of the half-space remains below 500 m/s in the eastern part.

## 5. QUALITATIVE COMPARISON OF VELOCITY MODELS AND RESULTING $V_P/V_S$

The comparison of velocity models obtained from P-wave tomography ($V_P^{tomo}$, Fig. 6a), SH-wave tomography ($V_S^{tomo}$, Fig. 6b), and surface-wave dispersion profiling ($V_S^{sw}$, Fig. 11) provided results that are consistent with the main structures interpreted from ERT data (Fig. 2b). However, velocity models do not provide such a clear delineation of these structures, especially for $V_P^{tomo}$ and $V_S^{tomo}$ sections. Indeed, the travel-time tomography method smoothes the lateral variations of velocity and often suffers from the strong influence of triggering issues on short travel times, which mainly affect the reconstruction of shallow structure velocities. As for surface-wave profiling, the overlaying of structures delimited by ERT on the $V_S^{sw}$ pseudo-2D section (Fig. 11) confirms the lateral consistency of both $V_S$ models in the first 20 m in depth. If the surface-wave method is clearly limited by its low investigation depth in this case, it provides more information regarding the lateral variations of shallow layers' velocities and seems to detect the modifications of mechanical properties occurring in the contact zone.

At both $Xmid$ = 50 m (Fig. 12a) and $Xmid$ = 402 m (Fig. 12d), 1D models of $V_S$ and $V_P$ extracted from tomography sections ($V_S^{tomo}$ in green solid line and $V_P^{tomo}$ in green dashed line, respectively) are characterized by similar trends of continuously increasing velocities in depth.

Furthermore, 1D $V_S^{sw}$ models (red solid line) show the presence of two constant velocity layers followed by a linearly increasing velocity layer overlaying the half-space. Despite a low investigation depth, the $V_S^{sw}$ pseudo-section manages to depict the shallow lateral variations and remains in good agreement with $V_S^{tomo}$.

As a control of both $V_S$ models, forward modelling was performed along the line (examples for $Xmid = 50$ m and $Xmid = 402$ m are shown in Fig. 12c and 12f, respectively). On the one hand, theoretical dispersion curves were computed using 1D $V_P^{tomo}$ and $V_S^{tomo}$ models (green solid line). On the other hand, theoretical dispersion curves were calculated using 1D $V_S^{sw}$ models and 1D $V_P^{tomo}$ models resampled in depth according to the $V_S^{sw}$ layering ($V_P^{rs}$) (red solid line). $V_S^{sw}$ models provide the best fit with the picked dispersion curves and the coherent maxima observed on dispersion images, supporting the validity of the final $V_S^{sw}$ model averaged from all models fitting the error bars. For their part, dispersion curves computed from $V_S^{tomo}$ models are generally not well fitting the observed propagation modes at low frequency, leading us to question the validity of the tomographic model in the deepest layers.

After cross-validating both $V_S$ models, we computed $V_P/V_S$ ratios along the line with: (i) $V_S^{sw}$ and $V_P^{rs}$ (Fig. 13a) and (ii) $V_S^{tomo}$ and $V_P^{tomo}$ (Fig. 13b). The $V_S^{tomo}/V_P^{tomo}$ section shows smooth lateral variations, with low $V_P/V_S$ ($\sim$ 1.5) in the western (from 0 m to 150 m) and central (from 200 m to 250 m) parts, separated by intermediate values ($\sim$ 2–2.5). The eastern part is characterized by higher values (around 2.5 and up to 3.5). At first sight, the $V_S^{sw}/V_P^{rs}$ section might look different, especially in the beginning of the line (from 0 m to 275 m), where anomalous high $V_P/V_S$ values are observed around 5-m to 10-m depth. At these depths, the $V_S^{sw}$ model presents mostly constant velocities, whereas the $V_P^{rs}$ model is characterized by linearly increasing velocities. This incompatibility can thus explain the $V_P/V_S$ discrepancies observed in this layer. With this in mind, we were yet able to delineate different $V_P/V_S$ areas, which correspond well to those observed on the $V_S^{tomo}/V_P^{tomo}$ section. These different areas and the observed $V_P/V_S$ values are also consistent with the main structures delineated in the ERT results (Fig. 2b), whereas it was not clear on $V_P$ or $V_S$ only.

Moreover, 1D $V_P/V_S$ ratios extracted at $Xmid = 50$ m (Fig. 12b) and $Xmid = 402$ m (Fig. 12e) from $V_P^{rs}/V_S^{sw}$ (red solid line) and $V_P^{tomo}/V_S^{tomo}$ (green solid line) show similar trends. Stronger contrasts and higher ratio values are yet observed on surface-wave analysis results. $V_P/V_S$ values

observed at $Xmid = 50$ m are overall low (below 2.75) with both methods. The water table level extrapolated from the nearest representative piezometric well implanted in the granite (around 100 m west from $Xmid = 50$ m) is not consistent with any of the contrasts observed on the $V_P/V_S$ models. Indeed, the estimated water table level ($\sim$ 20 m) is close to the maximum HSD where $V_S^{sw}$ becomes poorly resolved. Furthermore, no strong $V_P/V_S$ variations can be anticipated in such low-permeability and low-porosity materials (Takei 2002). At $Xmid = 402$ m, shallow high $V_P/V_S$ ratio values (around 4) are consistent with a wet soil, whereas a strong contrast at 11.5-m depth remarkably matches the water table level interpolated from levels measured in MF2 and F36 (black dashed line). This feature is confirmed on the pseudo-2D $V_P/V_S$ section in the eastern part (Fig. 13a).

## 6. DISCUSSION AND CONCLUSIONS

In order to assess the applicability of combined P-wave refraction tomography and surface-wave dispersion analysis to estimate $V_P/V_S$ ratio in near-surface applications, we performed seismic measurements on a well-known granite–micaschists contact at Plœmeur hydrological observatory (France). A simultaneous P- and surface-wave survey was achieved using a single acquisition set-up and was supplemented with an SH-wave acquisition along the same line in order to compare $V_S$ results obtained from SH-wave refraction tomography and surface-wave profiling.

P- and SH-wave first arrivals observed along the line were used to perform travel-time tomography and retrieve $V_P^{tomo}$ and $V_S^{tomo}$ models. Evenly spaced dispersion data were extracted along the line from P-wave shot gathers using windowing and stacking techniques. Successive 1D Monte Carlo inversions of these dispersion data were achieved using fixed $V_P$ values extracted from the $V_P^{tomo}$ model and no lateral constraints between two adjacent 1D inversions. The resulting 1D $V_S^{sw}$ models were then assembled to create a pseudo-2D $V_S^{sw}$ section. We computed normalized residuals between observed and calculated phase velocities along the line to control the quality of the $V_S^{sw}$ model. This model appears to be correctly matching the $V_S^{tomo}$ model obtained with SH-wave refraction tomography. The $V_S^{sw}$ model is however characterized by strong velocity uncertainties in the deepest layers. The recomputation of theoretical dispersion curves along the line also provided results that are consistent with the measured dispersion images and proved to be a reliable tool for validating $V_S$ models obtained from SH-wave refraction tomography and surface-wave profiling. Finally, we

were able to compute $V_P/V_S$ sections from both $V_S^{sw}$ and $V_S^{tomo}$. The two sections present similar features, but the section obtained from $V_S^{sw}$ shows a higher lateral resolution, which is consistent with the features observed on ERT, thus validating our approach for retrieving $V_P/V_S$ ratio from combined P-wave tomography and surface-wave profiling. Furthermore, the $V_P/V_S$ ratios obtained in the clay and micaschists area show a strong contrast consistent with the observed water table level.

An incompatibility, however, remains between $V_P^{rs}$ and $V_S^{sw}$, which can lead to anomalous $V_P/V_S$ values. Indeed, travel-time tomography provides a smooth 2D reconstruction of the medium along ray paths propagating from sources to sensors in a narrow frequency band. The investigation depth is strongly related to the length of the acquisition profile and the maximum offset between sources and receivers. Furthermore, the medium is described as a function of the ray coverage, which is strongly related to the spacing between sensors and usually increases in high-velocity zones. For their part, surface-wave methods allow reconstructing pseudo-2D $V_S$ sections by juxtaposing single 1D models obtained along the line. In this case, the spectral resolution and the investigation depth are a function of the frequency and increase with the length of the recording array, whereas the lateral resolution is inversely correlated with the individual array length. In order to retrieve $V_P$ and $V_S$ models more suited for $V_P/V_S$ computation, a joint inversion approach combining Rayleigh and P-guided waves dispersion data along with P-wave refraction travel times could be developed, in the continuation of Maraschini *et al.* (2010), Piatti *et al.* (2013) and Boiero, Wiarda, and Vermeer (2013b) works.

## 7. ACKNOWLEDGEMENTS

The authors would like to thank Claudio Strobbia, Daniela Donno, and two anonymous reviewers for their constructive comments. This work was supported by the French National Programme EC2CO – Biohefect (Project "Études expérimentales multi-échelles de l'apport des vitesses sismiques à la description du continuum sol-aquifère") and the ANR Project CRITEX ANR-11-EQPX-0011. It was also supported by the SOERE-H+ "Réseau National de sites hydrogéologiques" network and by the CLIMAWAT European Project "Adapting to the Impacts of Climate Change on Groundwater Quantity and Quality". They kindly thank A. Kehil, J. Jimenez-Martinez, E. Coulon, and N. Lavenant (Géosciences Rennes) for technical assistance during field work. They would also like to

thank J. Thiesson (UMR METIS) for valuable discussions during data processing and interpretation.

## 8. REFERENCES


Bauer K., Moeck I., Norden B., Schulze A., Weber M. and Wirth H. 2010. Tomographic P wave velocity and vertical velocity gradient structure across the geothermal site Groß Schönebeck (NE German Basin): relationship to lithology, salt tectonics, and thermal regime. *Journal of Geophysical Research: Solid Earth* **115**(B8), B08312.

Bauer K., Schulze A., Ryberg T., Sobolev S.V. and Weber M.H. 2003. Classification of lithology from seismic tomography: a case study from the Messum igneous complex, Namibia. *Journal of Geophysical Research: Solid Earth* **108**(B3), 2152.

Baumann-Wilke M., Bauer K., Schovsbo N.H. and Stiller M. 2012. P-wave traveltime tomography for a seismic characterization of black shales at shallow depth on Bornholm, Denmark. *Geophysics* **77**(5), EN53–EN60.

Bergamo P., Boiero D. and Socco L.V. 2012. Retrieving 2D structures from surface-wave data by means of space-varying spatial windowing. *Geophysics* **77**(4), EN39–EN51.

Berryman J.G. 1999. Origin of Gassmann's equations. *Geophysics* **64**(5), 1627–1629.

Biot M.A. 1956a. Theory of propagation of elastic waves in a fluid-saturated porous solid. I. Low-frequency range. *The Journal of the Acoustical Society of America* **28**(2), 168–178.

Biot M.A. 1956b. Theory of propagation of elastic waves in a fluid-saturated porous solid. II. Higher frequency range. *The Journal of the Acoustical Society of America* **28**(2), 179–191.

Boaga J., Cassiani G., Strobbia C. and Vignoli G. 2013. Mode misidentification in Rayleigh waves: ellipticity as a cause and a cure. *Geophysics* **78**(4), EN17–EN28.

Bodet L. 2005. *Limites théoriques et expérimentales de l'interprétation de la dispersion des ondes de Rayleigh: apport de la modélisation numérique et physique*. PhD thesis, École Centrale de Nantes et Université de Nantes, France.

Bodet L., Abraham O. and Clorennec D. 2009. Near-offset effects on Rayleigh-wave dispersion measurements: physical modeling. *Journal of Applied Geophysics* **68**(1), 95–103.

Bodet L., van Wijk K., Bitri A., Abraham O., Côte P., Grandjean G. *et al.* 2005. Surface-wave inversion limitations from laser-Doppler physical modeling. *Journal of Environmental and Engineering Geophysics* **10**(2), 151–162.

Bohlen T., Kugler S., Klein G. and Theilen F. 2004. 1.5D inversion of lateral variation of Scholte-wave dispersion. *Geophysics* **69**(2), 330–344.

Boiero D. and Socco L.V. 2010. Retrieving lateral variations from surface wave dispersion curves. *Geophysical Prospecting* **58**(6), 977–996.

Boiero D. and Socco L.V. 2011. The meaning of surface wave dispersion curves in weakly laterally varying structures. *Near Surface Geophysics* **9**(6), 561–570.

Boiero D., Socco L.V., Stocco S. and Wisén R. 2013a. Bedrock mapping in shallow environments using surface-wave analysis. *The Leading Edge* **32**(6), 664–672.

Boiero D., Wiarda E. and Vermeer P. 2013b. Surface- and guided-wave inversion for near-surface modeling in land and shallow marine seismic data. *The Leading Edge* **32**(6), 638–646.

Cardarelli E., Cercato M. and De Donno G. 2014. Characterization of an earth-filled dam through the combined use of electrical resistivity tomography, P- and SH-wave seismic tomography and surface wave data. *Journal of Applied Geophysics* **106**, 87–95.

509 Catchings R.D. 1999. Regional Vp, Vs, Vp/Vs, and Poisson's ratios across earthquake source zones from Memphis,
510 Tennessee, to St. Louis, Missouri. *Bulletin of the Seismological Society of America* **89**(6), 1591–1605.
511 Der Z.A. and Landisman M. 1972. Theory for errors, resolution, and separation of unknown variables in inverse
512 problems, with application to the mantle and the crust in southern Africa and Scandinavia. *Geophysical Journal of*
513 *the Royal Astronomical Society* **27**(2), 137–178.
514 Dvorkin J. 2008. Yet another Vs equation. *Geophysics* **73**(2), E35–E39.
515 Endrun B., Meier T., Lebedev S., Bohnhoff M., Stavrakakis G. and Harjes H.P. 2008. S velocity structure and radial
516 anisotropy in the Aegean region from surface wave dispersion. *Geophysical Journal International* **174**(2), 593–616.
517 Ezersky M.G., Bodet L., Akawwi E., Al-Zoubi A.S., Camerlynck C., Dhemaied A. *et al.* 2013. Seismic surface-wave
518 prospecting methods for sinkhole hazard assessment along the Dead Sea shoreline. *Journal of Environmental and*
519 *Engineering Geophysics* **18**(4), 233–253.
520 Fabien-Ouellet G. and Fortier R. 2014. Using all seismic arrivals in shallow seismic investigations. *Journal of Applied*
521 *Geophysics* **103**, 31–42.
522 Forbriger T. 2003a. Inversion of shallow-seismic wavefields: I. Wavefield transformation. *Geophysical Journal*
523 *International* **153**(3), 719–734.
524 Forbriger T. 2003b. Inversion of shallow-seismic wavefields: II. Inferring subsurface properties from wavefield transforms.
525 *Geophysical Journal International* **153**(3), 735–752.
526 Fu D.T., Sullivan E.C. and Marfurt K.J. 2006. Rock-property and seismic-attribute analysis of a chert reservoir in
527 the Devonian Thirty-one Formation, west Texas, U.S.A. *Geophysics* **71**(5), B151–B158.
528 Gabriels P., Snieder R. and Nolet G. 1987. In situ measurements of shear-wave velocity in sediments with higher-mode
529 Rayleigh waves. *Geophysical Prospecting* **35**(2), 187–196.
530 Galibert P.Y., Valois R., Mendes M. and Guérin R. 2014. Seismic study of the low-permeability volume in southern
531 France karst systems. *Geophysics* **79**(1), EN1–EN13.
532 Gautier S., Latorre D., Virieux J., Deschamps A., Skarpelos C., Sotiriou A. *et al.* 2006. A new passive tomography of
533 the Aigion area (Gulf of Corinth, Greece) from the 2002 data set. *Pure and Applied Geophysics* **163**(2–3), 431–453.
534 Gibson B.S., Odegard M.E. and Sutton G.H. 1979. Nonlinear least-squares inversion of traveltime data for a linear
535 velocity-depth relationship. *Geophysics* **44**(2), 185–194.
536 Godio A., Strobbia C. and De Bacco G. 2006. Geophysical characterisation of a rockslide in an alpine region.
537 *Engineering Geology* **83**(1–3), 273–286.
538 Grandjean G. and Bitri A. 2006. 2M-SASW : Multifold multichannel seismic inversion of local dispersion of Rayleigh
539 waves in laterally heterogeneous subsurfaces: application to the Super-Sauze earthflow, France. *Near Surface*
540 *Geophysics* **4**(6), 367–375.
541 Grelle G. and Guadagno F.M. 2009. Seismic refraction methodology for groundwater level determination: "Water
542 seismic index". *Journal of Applied Geophysics* **68**(3), 301–320.
543 Haines S. 2007. A hammer-impact, aluminium, shear-wave seismic source. Technical Report OF 07-1406. United
544 States Geological Survey.
545 Haney M.M. and Douma H. 2012. Rayleigh-wave tomography at Coronation Field, Canada: The topography effect.
546 *The Leading Edge* **31**(1), 54–61.

547 Haskell N.A. 1953. The dispersion of surface waves on multilayered media. *Bulletin of the Seismological Society of*
548 *America* **43**(1), 17–34.
549 Hayashi K. and Suzuki H. 2004. CMP cross-correlation analysis of multi-channel surface-wave data. *Exploration*
550 *Geophysics* **35**(1), 7–13.
551 Heitor A., Indraratna B., Rujikiatkamjorn C. and Golaszewski R. 2012. Characterising compacted fills at Penrith
552 Lakes development site using shear wave velocity and matric suction. In: *11th Australia - New Zealand Conference*
553 *on Geomechanics: Ground Engineering in a Changing World*, Melbourne, Australia. pp. 1262–1267.
554 Hibert C., Grandjean G., Bitri A., Travelletti J. and Malet J.P. 2012. Characterizing landslides through geophysical
555 data fusion: Example of the La Valette landslide (France). *Engineering Geology* **128**, 23–29.
556 Ikeda T., Tsuji T. and Matsuoka T. 2013. Window-controlled CMP crosscorrelation analysis for surface waves in
557 laterally heterogeneous media. *Geophysics* **78**(6), EN95–EN105.
558 Ivanov J., Miller R.D., Xia J., Steeples D. and Park C.B. 2006. Joint analysis of refractions with surface waves: an
559 inverse solution to the refraction-traveltime problem. *Geophysics* **71**(6), R131–R138.
560 Jiménez-Martínez J., Longuevergne L., Le Borgne T., Davy P., Russian A. and Bour O. 2013. Temporal and spatial
561 scaling of hydraulic response to recharge in fractured aquifers: Insights from a frequency domain analysis. *Water*
562 *Resources Research* **49**(5), 3007–3023.
563 Jongmans D. 1992. The application of seismic methods for dynamic characterization of soils in earthquake engineering.
564 *Bulletin of the International Association of Engineering Geology - Bulletin de l'Association Internationale de*
565 *Géologie de l'Ingénieur* **46**(1), 63–69.
566 Jongmans D., Bièvre G., Renalier F., Schwartz S., Beaurez N. and Orengo Y. 2009. Geophysical investigation of a
567 large landslide in glaciolacustrine clays in the Trièves area (French Alps). *Engineering Geology* **109**(1–2), 45–56.
568 Jongmans D. and Demanet D. 1993. The importance of surface waves in vibration study and the use of Rayleigh
569 waves for estimating the dynamic characteristics of soils. *Engineering Geology* **34**(1–2), 105–113.
570 Julià J. and Mejía J. 2004. Thickness and Vp/Vs ratio variation in the Iberian crust. *Geophysical Journal International*
571 **156**(1), 59–72.
572 Konstantaki L., Carpentier S., Garofalo F., Bergamo P. and Socco L.V. 2013. Determining hydrological and soil
573 mechanical parameters from multichannel surface-wave analysis across the Alpine Fault at Inchbonnie, New Zealand.
574 *Near Surface Geophysics* **11**(4), 435–448.
575 Lai C.G. and Rix G.J. 1998. Simultaneous inversion of Rayleigh phase velocity and attenuation for near-surface site
576 characterization. Report No. GIT-CEE/GEO-98-2. Georgia Institute of Technology.
577 Latorre D., Virieux J., Monfret T., Monteiller V., Vanorio T., Got J.L. *et al.* 2004. A new seismic tomography of
578 Aigion area (Gulf of Corinth, Greece) from the 1991 data set. *Geophysical Journal International* **159**(3), 1013–1031.
579 Le Borgne T., Bour O., Paillet F.L. and Caudal J.P. 2006a. Assessment of preferential flow path connectivity and
580 hydraulic properties at single-borehole and cross-borehole scales in a fractured aquifer. *Journal of Hydrology*
581 **328**(1–2), 347–359.
582 Le Borgne T., Bour O., Riley M.S., Gouze P., Pezard P.A., Belghoul A. *et al.* 2007. Comparison of alternative
583 methodologies for identifying and characterizing preferential flow paths in heterogeneous aquifers. *Journal of*
584 *Hydrology* **345**(3–4), 134–148.

585 Le Borgne T., Paillet F., Bour O. and Caudal J.P. 2006b. Cross-borehole flowmeter tests for transient heads in
586 heterogeneous aquifers. *Ground Water* **44**(3), 444–452.
587 Lee M.W. 2002. Modified Biot-Gassmann theory for calculating elastic velocities for unconsolidated and consolidated
588 sediments. *Marine Geophysical Researches* **23**(5–6), 403–412.
589 Lees J.M. and Wu H. 2000. Poisson's ratio and porosity at Coso geothermal area, California. *Journal of Volcanology*
590 *and Geothermal Research* **95**(1–4), 157–173.
591 Loke M.H. and Barker R.D. 1996. Rapid least-squares inversion of apparent resistivity pseudosections by a quasi-
592 Newton method. *Geophysical Prospecting* **44**(1), 131–152.
593 Maraschini M., Ernst F., Foti S. and Socco L.V. 2010. A new misfit function for multimodal inversion of surface
594 waves. *Geophysics* **75**(4), G31–G43.
595 McNeill J. 1980. Electromagnetic terrain conductivity measurement at low induction numbers. Technical Report
596 TN-6. Geonics Limited. Ontario, Canada.
597 Mokhtar T.A., Herrmann R.B. and Russell D.R. 1988. Seismic velocity and Q model for the shallow structure of the
598 Arabian Shield from short-period Rayleigh waves. *Geophysics* **53**(11), 1379–1387.
599 Mota R. and Monteiro Santos F. 2010. 2D sections of porosity and water saturation from integrated resistivity and
600 seismic surveys. *Near Surface Geophysics* **8**(6), 575–584.
601 Murphy W.F.I. 1982. Effects of partial water saturation on attenuation in Massillon sandstone and Vycor porous
602 glass. *The Journal of the Acoustical Society of America* **71**(6), 1458–1468.
603 Nakajima J., Matsuzawa T., Hasegawa A. and Zhao D. 2001. Three-dimensional structure of Vp, Vs, and Vp/Vs
604 beneath northeastern Japan: Implications for arc magmatism and fluids. *Journal of Geophysical Research: Solid*
605 *Earth* **106**(B10), 21843–21857.
606 Neducza B. 2007. Stacking of surface waves. *Geophysics* **72**(2), 51–58.
607 Nicholson C. and Simpson D.W. 1985. Changes in Vp/Vs with depth: implications for appropriate velocity models,
608 improved earthquake locations, and material properties of the upper crust. *Bulletin of the Seismological Society of*
609 *America* **75**(4), 1105–1123.
610 Olona J., Pulgar J., Fernández-Viejo G., López-Fernández C. and González-Cortina J. 2010. Weathering variations
611 in a granitic massif and related geotechnical properties through seismic and electrical resistivity methods. *Near*
612 *Surface Geophysics* **8**(6), 585–599.
613 O'Neill A. 2003. *Full-waveform reflectivity for modelling, inversion and appraisal of seismic surface wave dispersion*
614 *in shallow site investigations*. PhD thesis, The University of Western Australia, Australia.
615 O'Neill A., Dentith M. and List R. 2003. Full-waveform P-SV reflectivity inversion of surface waves for shallow
616 engineering applications. *Exploration Geophysics* **34**(3), 158–173.
617 O'Neill A. and Matsuoka T. 2005. Dominant higher surface-wave modes and possible inversion pitfalls. *Journal of*
618 *Environmental and Engineering Geophysics* **10**(2), 185–201.
619 Othman A.A.A. 2005. Construed geotechnical characteristics of foundation beds by seismic measurements. *Journal*
620 *of Geophysics and Engineering* **2**(2), 126–138.
621 Park C.B., Miller R.D. and Xia J. 1999. Multichannel analysis of surface waves. *Geophysics* **64**(3), 800–808.
622 Pasquet S., Bodet L., Dhemaied A., Mouhri A., Vitale Q., Rejiba F. *et al.* 2015. Detecting different water table

levels in a shallow aquifer with combined P-, surface and SH-wave surveys: insights from Vp/Vs or Poisson's ratios. *Journal of Applied Geophysics* **113**, 38–50.

Pasquet S., Bodet L., Longuevergne L., Dhemaied A., Rejiba F., Camerlynck C. *et al.* 2012. Surface-wave dispersion stacking on a granite-micaschists contact at Ploemeur hydrological observatory, France. In: *Near Surface Geoscience 2012 – 18th European Meeting of Environmental and Engineering Geophysics*, Paris, France. EAGE.

Pasquet S., Sauvin G., Andriamboavonjy M.R., Bodet L., Lecomte I. and Guérin R. 2014. Surface-wave dispersion inversion versus SH-wave refraction tomography in saturated and poorly dispersive quick clays. In: *Near Surface Geoscience 2014 – 20th European Meeting of Environmental and Engineering Geophysics*, Athens, Greece. EAGE.

Pérez Solano C.A. 2013. *Two-dimensional near-surface seismic imaging with surface waves: alternative methodology for waveform inversion*. PhD thesis, École Nationale Supérieure des Mines de Paris, France.

Pérez Solano C.A.P., Donno D. and Chauris H. 2014. Alternative waveform inversion for surface wave analysis in 2-D media. *Geophysical Journal International* **198**(3), 1359–1372.

Piatti C., Socco L., Boiero D. and Foti S. 2013. Constrained 1D joint inversion of seismic surface waves and P-refraction traveltimes. *Geophysical Prospecting* **61**(1), 77–93.

Powell C.A., Withers M.M., Cox R.T., Vlahovic G. and Arroucau P. 2014. Crustal velocity structure associated with the eastern Tennessee seismic zone: Vp and Vs images based upon local earthquake tomography. *Journal of Geophysical Research: Solid Earth* **119**(1), 464–489.

Prasad M. 2002. Acoustic measurements in unconsolidated sands at low effective pressure and overpressure detection. *Geophysics* **67**(2), 405–412.

Raptakis D., Chávez-García F.J., Makra K. and Pitilakis K. 2000. Site effects at Euroseistest—I. Determination of the valley structure and confrontation of observations with 1D analysis. *Soil Dynamics and Earthquake Engineering* **19**(1), 1–22.

Renalier F., Jongmans D., Savvaidis A., Wathelet M., Endrun B. and Cornou C. 2010. Influence of parameterization on inversion of surface wave dispersion curves and definition of an inversion strategy for sites with a strong contrast. *Geophysics* **75**(6), B197–B209.

Reyners M., Eberhart-Phillips D., Stuart G. and Nishimura Y. 2006. Imaging subduction from the trench to 300 km depth beneath the central North Island, New Zealand, with Vp and Vp/Vs. *Geophysical Journal International* **165**(2), 565–583.

Rohdewald S.R. 2011. Interpretation of first-arrival travel times with wavepath eikonal traveltime inversion and wavefront refraction method. In: *Symposium on the Application of Geophysics to Engineering and Environmental Problems*, Charleston, SC, p. 13. EEGS.

Rojas E. 2008. Vp-Vs ratio sensitivity to pressure, fluid, and lithology changes in tight gas sandstones. *First Break* **26**(3), 83–86.

Ruelleu S., Moreau F., Bour O., Gapais D. and Martelet G. 2010. Impact of gently dipping discontinuities on basement aquifer recharge: an example from Ploemeur (Brittany, France). *Journal of Applied Geophysics* **70**(2), 161–168.

Russel D.R. 1987. *Multi-channel processing of dispersed surface waves*. PhD thesis, Saint Louis University, USA.

Ryberg T., Hole J.A., Fuis G.S., Rymer M.J., Bleibinhaus F., Stromeyer D. *et al.* 2012. Tomographic Vp and Vs structure of the California Central Coast Ranges, in the vicinity of SAFOD, from controlled-source seismic data.

*Geophysical Journal International* **190**(3), 1341–1360.

Sambridge M. 1999. Geophysical inversion with a neighbourhood algorithm—I. Searching a parameter space. *Geophysical Journal International* **138**(2), 479–494.

Sambuelli L., Deidda G.P., Albis G., Giorcelli E. and Tristano G. 2001. Comparison of standard horizontal geophones and newly designed horizontal detectors. *Geophysics* **66**(6), 1827–1837.

Sanders C.O., Ponko S.C., Nixon L.D. and Schwartz E.A. 1995. Seismological evidence for magmatic and hydrothermal structure in Long Valley Caldera from local earthquake attenuation and velocity tomography. *Journal of Geophysical Research: Solid Earth* **100**(B5), 8311–8326.

Schuster G.T. and Quintus-Bosz A. 1993. Wavepath eikonal traveltime inversion: theory. *Geophysics* **58**(9), 1314–1323.

Schutt D.L. and Humphreys E.D. 2004. P and S wave velocity and Vp/Vs in the wake of the Yellowstone hot spot. *Journal of Geophysical Research: Solid Earth* **109**(B1), B01305.

Sheehan J.R., Doll W.E. and Mandell W.A. 2005. An evaluation of methods and available software for seismic refraction tomography analysis. *Journal of Environmental and Engineering Geophysics* **10**(1), 21–34.

Sheriff R.E. and Geldart L.P. 1995. *Exploration Seismology*, 2 edn. Cambridge University Press.

Socco L.V., Foti S. and Boiero D. 2010a. Surface-wave analysis for building near-surface velocity models - Established approaches and new perspectives. *Geophysics* **75**(5), A83–A102.

Socco L.V., Jongmans D., Boiero D., Stocco S., Maraschini M., Tokeshi K. *et al.* 2010b. Geophysical investigation of the Sandalp rock avalanche deposits. *Journal of Applied Geophysics* **70**(4), 277–291.

Socco L.V. and Strobbia C. 2004. Surface-wave method for near-surface characterization: a tutorial. *Near Surface Geophysics* **2**(4), 165–185.

Strobbia C. and Foti S. 2006. Multi-offset phase analysis of surface wave data (MOPA). *Journal of Applied Geophysics* **59**(4), 300–313.

Strobbia C., Laake A., Vermeer P. and Glushchenko A. 2011. Surface waves: use them then lose them. Surface-wave analysis, inversion and attenuation in land reflection seismic surveying. *Near Surface Geophysics* **9**(6), 503–514.

Takei Y. 2002. Effect of pore geometry on Vp/Vs: From equilibrium geometry to crack. *Journal of Geophysical Research: Solid Earth* **107**(B2), 2043.

Tatham R.H. 1982. Vp/Vs and lithology. *Geophysics* **47**(3), 336–344.

Tatham R.H. and Stoffa P.L. 1976. Vp/Vs—A potential hydrocarbon indicator. *Geophysics* **41**(5), 837–849.

Thompson T. and Evans B. 2000. Stress-induced anisotropy: the effects of stress on seismic wave propagation. *Exploration Geophysics* **31**(3), 489.

Thomson W.T. 1950. Transmission of elastic waves through a stratified solid medium. *Journal of Applied Physics* **21**(2), 89–93.

Touchard F. 1999. *Caractérisation hydrogéologique d'un aquifère en socle fracturé - Site de Ploemeur (Morbihan)*. PhD thesis, Géosciences Rennes, France.

Tryggvason A. and Linde N. 2006. Local earthquake (LE) tomography with joint inversion for P- and S-wave velocities using structural constraints. *Geophysical Research Letters* **33**(7), L07303.

Turesson A. 2007. A comparison of methods for the analysis of compressional, shear, and surface wave seismic data, and determination of the shear modulus. *Journal of Applied Geophysics* **61**(2), 83–91.

699 Uyanık O. 2011. The porosity of saturated shallow sediments from seismic compressional and shear wave velocities.
700 *Journal of Applied Geophysics* **73**(1), 16–24.
701 Vignoli G. and Cassiani G. 2010. Identification of lateral discontinuities via multi-offset phase analysis of surface
702 wave data. *Geophysical Prospecting* **58**(3), 389–413.
703 Walck M.C. 1988. Three-dimensional Vp/Vs variations for the Coso Region, California. *Journal of Geophysical*
704 *Research: Solid Earth* **93**(B3), 2047–2052.
705 Wathelet M. 2008. An improved neighborhood algorithm: parameter conditions and dynamic scaling. *Geophysical*
706 *Research Letters* **35**(9), L09301.
707 Wathelet M., Jongmans D. and Ohrnberger M. 2004. Surface-wave inversion using a direct search algorithm and its
708 application to ambient vibration measurements. *Near Surface Geophysics* **2**(4), 211–221.
709 Wilkens R., Simmons G. and Caruso L. 1984. The ratio Vp/Vs as a discriminant of composition for siliceous limestones.
710 *Geophysics* **49**(11), 1850–1860.
711 Wyllie M.R.J., Gregory A.R. and Gardner L.W. 1956. Elastic wave velocities in heterogeneous and porous media.
712 *Geophysics* **21**(1), 41–70.
713 Xia J., Miller R.D., Park C.B. and Tian G. 2003. Inversion of high frequency surface waves with fundamental and
714 higher modes. *Journal of Applied Geophysics* **52**(1), 45–57.
715 Xia J., Miller R.D., Park C.B., Wightman E. and Nigbor R. 2002. A pitfall in shallow shear-wave refraction surveying.
716 *Journal of Applied Geophysics* **51**(1), 1–9.
717 Zhang S.X. and Chan L.S. 2003. Possible effects of misidentified mode number on Rayleigh wave inversion. *Journal*
718 *of Applied Geophysics* **53**(1), 17–29.
719 Zywicki D. and Rix G. 2005. Mitigation of near-field effects for seismic surface wave velocity estimation with cylindrical
720 beamformers. *Journal of Geotechnical and Geoenvironmental Engineering* **131**(8), 970–977.

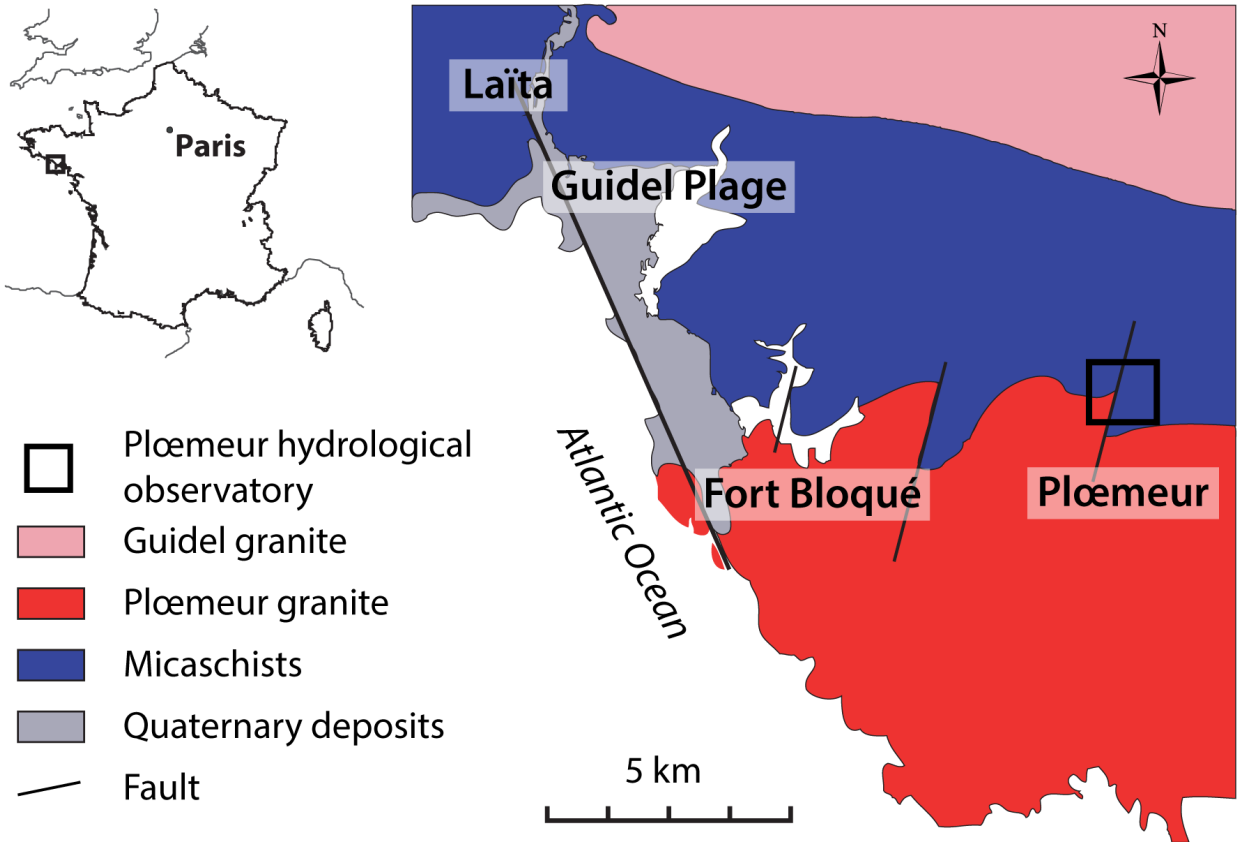


Figure 1: Geological context of the Plœmeur hydrological observatory and location of the experimentation (modified from Ruelleu *et al.* (2010) and Jiménez-Martínez *et al.* (2013)).

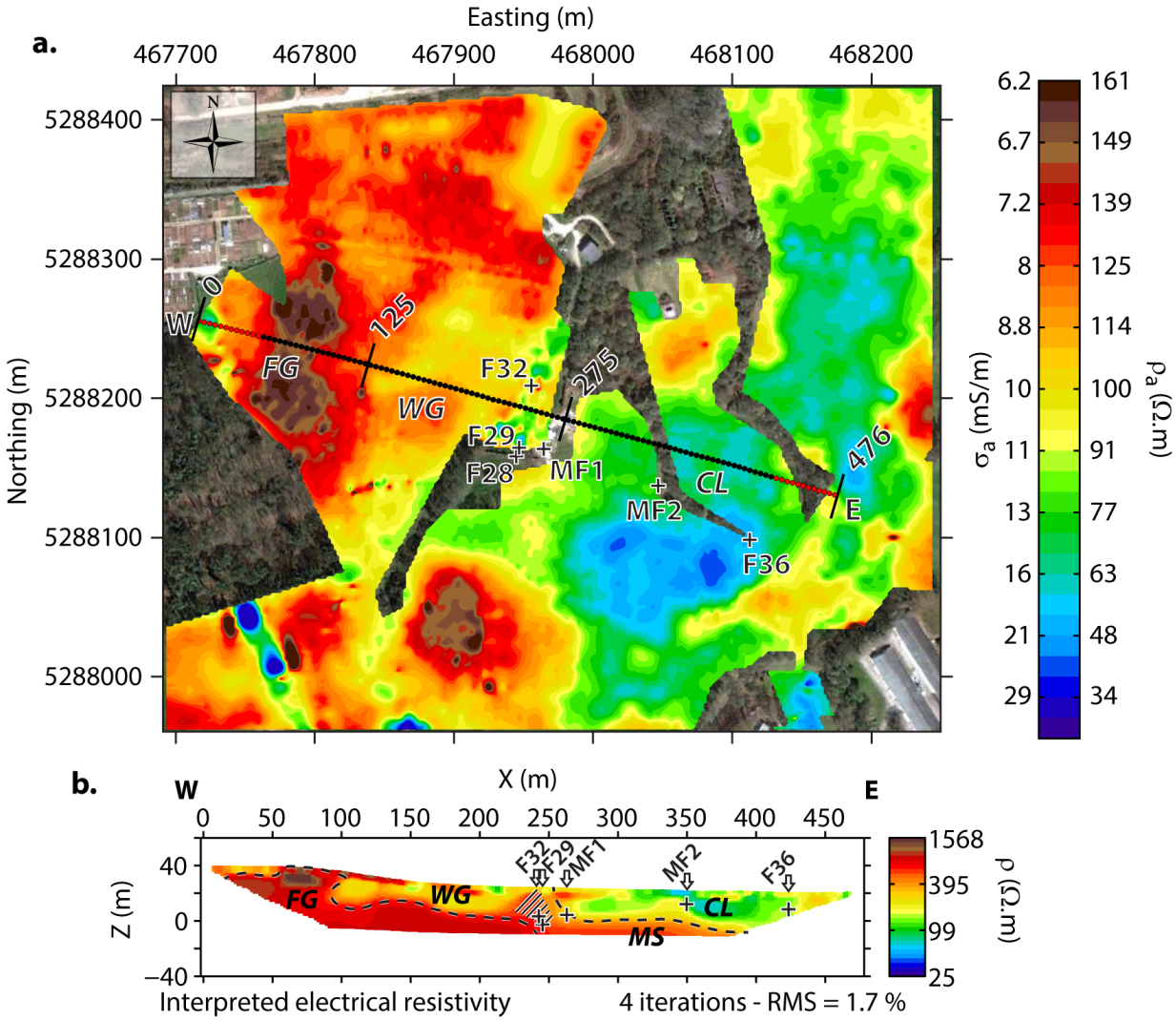


Figure 2: (a) Apparent EC values ($\sigma_a$) obtained from slingram EC mapping and location of the acquisition line (WE) for ERT and seismic measurements. Black dots between 30 m and 446 m represent the extent of the surface-wave analysis, whereas red dots represent the full extent of the survey. Locations of monitoring wells (F* and MF*) are represented with white crosses. (b) Electrical resistivity values ($\rho$) interpreted from ERT carried out along the WE line. Four main structures are delineated: fresh granite (FG), weathered granite (WG), clays (CL), and micaschists (MS). Markers at 125 m and 275 m in (a) delineate the three main shallow structures. The hashed area in (b) corresponds to a possible evidence of the contact zone. Positions of the nearest monitoring wells are projected along the WE line in (b) and represented with white arrows, pointing downwards to the corresponding piezometric head level (black crosses).

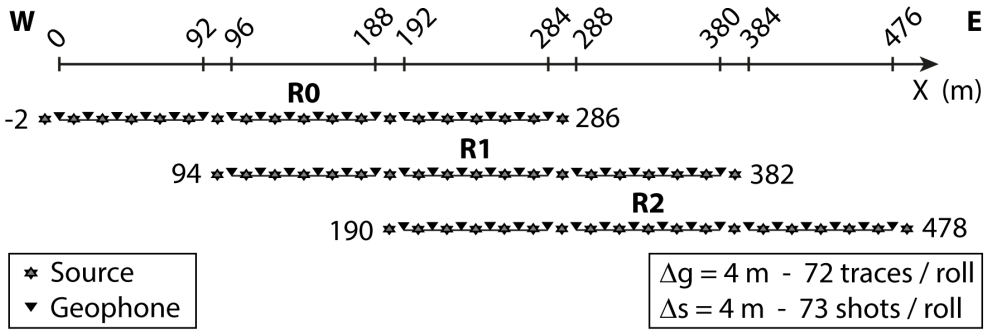


Figure 3: Seismic acquisition set-up used for combined P-, surface-, and SH-wave surveys. P- and surface-wave data were obtained using 72 14-Hz vertical geophones, whereas SH waves were recorded with 72 14-Hz horizontal geophones. Interval between two geophones ($\Delta g$) and move-up between shots ($\Delta s$) were both 4 m. We used one base roll (R0) and two roll-alongs (R1 and R2) of 72 traces each, with an overlap of 48 traces between two successive rolls, to obtain a 476-m-long profile. The origin of the $x$-axis is identical to the one used for ERT (Fig. 2b).

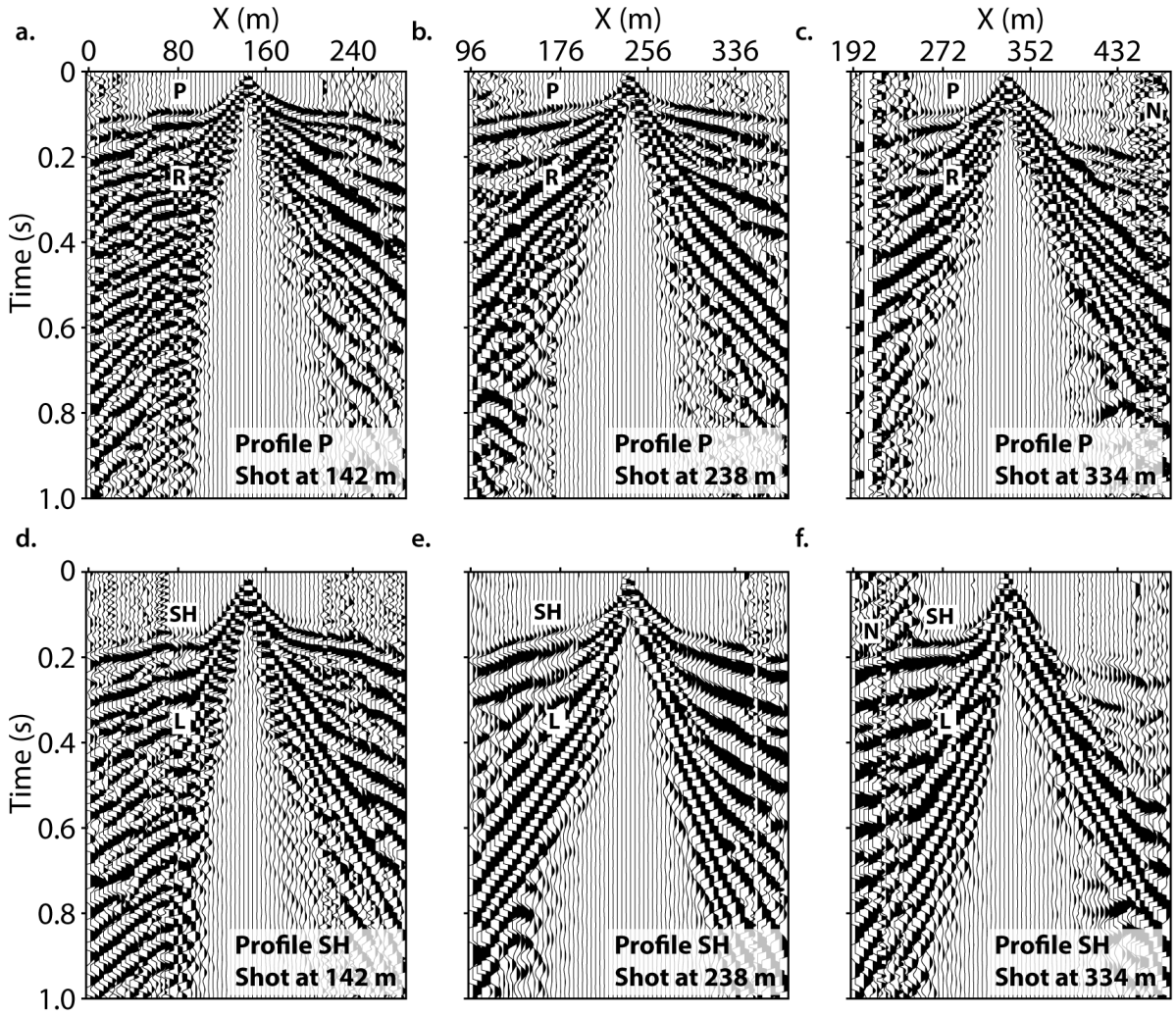


Figure 4: Seismograms for three shots recorded with vertical component geophones (profile P) and located at the centres of the base roll (a, $x = 142$ m), the first roll-along (b, $x = 238$ m), and the second roll-along (c, $x = 334$ m). Seismograms for three shots recorded with horizontal component geophones (profile SH) and located at the centres of the base roll (d, $x = 142$ m), the first roll-along (e, $x = 238$ m), and the second roll-along (f, $x = 334$ m). Data were only clipped over the $70^{\text{th}}$ percentile in amplitude. P-wave (P) and Rayleigh-wave (R) are observed on seismograms recorded with vertical geophones. SH-wave (SH) and Love-wave (L) are visible on seismograms recorded with horizontal geophones. Data are affected with significant noise level (N) at far offset.

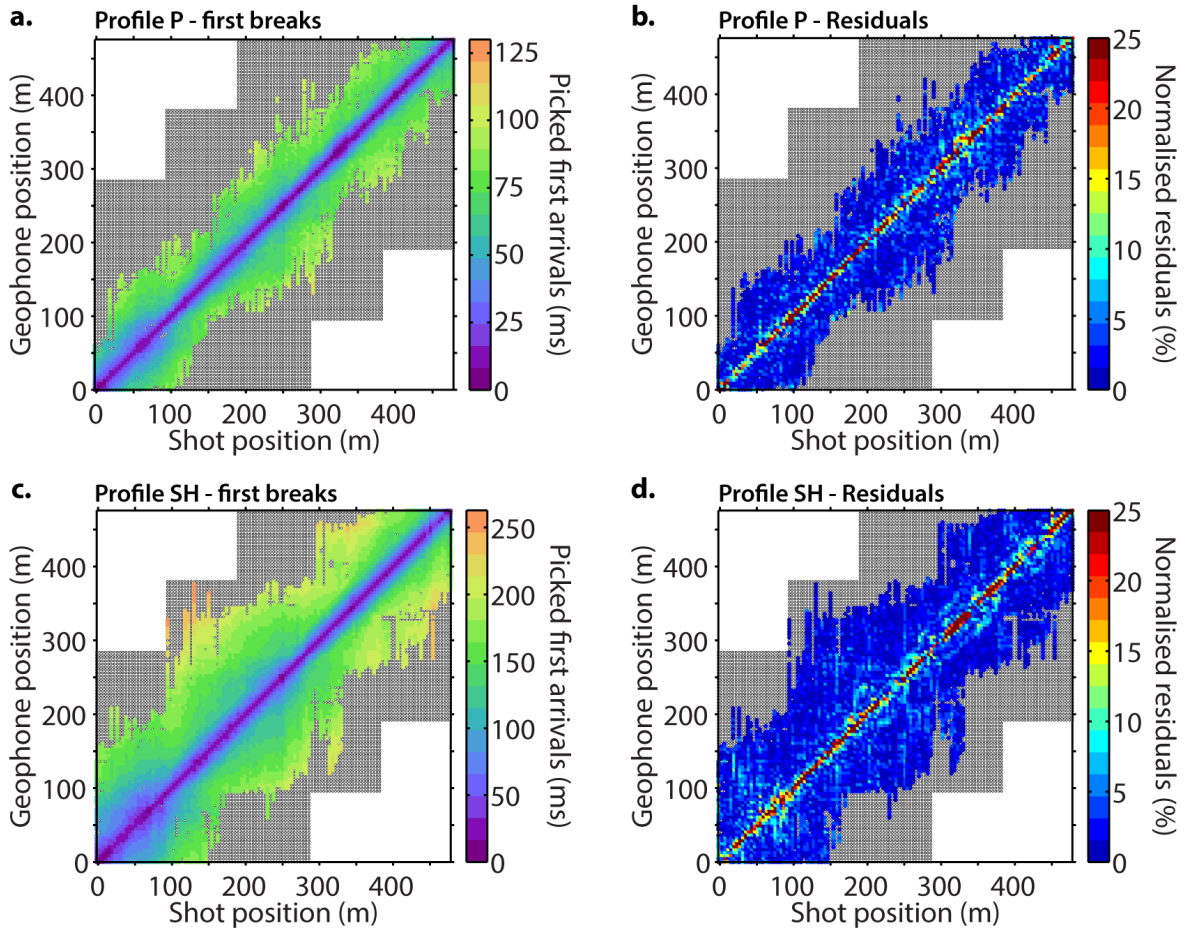


Figure 5: P-wave (a) and SH-wave (c) picked first arrival times and corresponding normalized residuals computed after P-wave (b) and SH-wave (d) tomography inversions, represented as a function of source and receiver distance. Black dots correspond to existing traces, whereas coloured dots represent picked traces. The diagonal trace (equal source and receiver location) indicates zero-offset travel times.

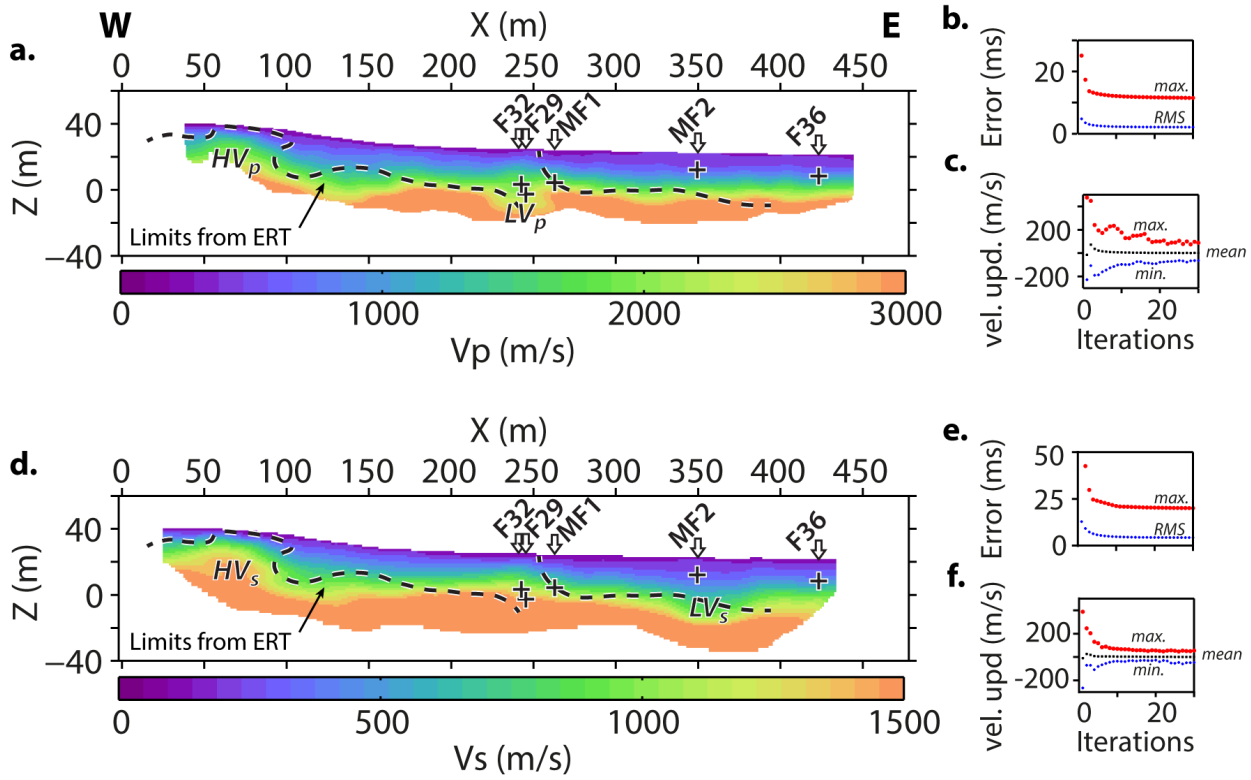


Figure 6: Final $V_P$ (a) and $V_S$ (d) models obtained after a total of 30 iterations, overlaid with limits interpreted from ERT results. The velocity models are clipped below a ray coverage of 100 rays per grid cell. The main features observed on the models are: (i) higher $V_P$ and $V_S$ in the western part ($HV_P$ and $HV_S$, respectively); (ii) lower $V_P$ in the centre ($LV_P$); and (iii) lower $V_S$ in the eastern part of the profile ($LV_S$). Changes of maximum normalized residual (in red) and global RMS error (in blue) are represented along the inversion process for $V_P$ (b) and $V_S$ (e) models. Maximum, minimum, and mean velocity updates (in red, blue, and black, respectively) are represented at each inversion iteration for $V_P$ (c) and $V_S$ (f) models. Positions of the nearest monitoring wells are projected along the WE line as in Fig. 2b.

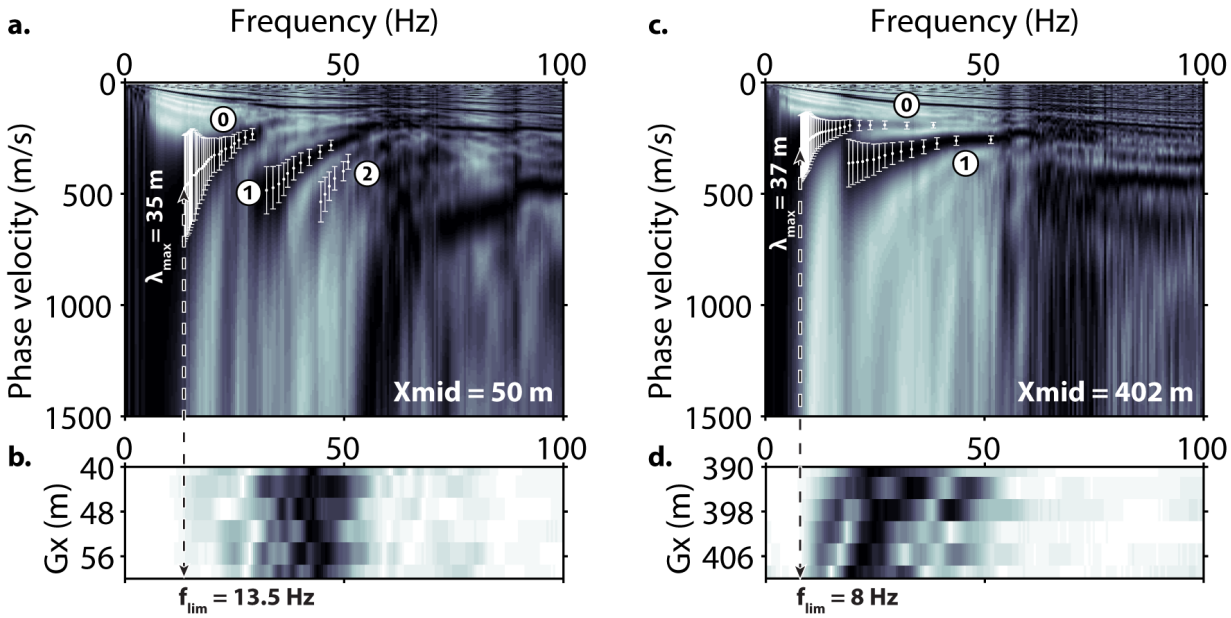


Figure 7: Dispersion images extracted on both sides of the seismic profile (a, $Xmid = 50$ m, and c, $Xmid = 402$ m) from six direct and six reverse shots with a six-trace (20-m-wide) window. $Xmid$ is the position of the spread mid-point along the line. Spectral amplitude of the far offset direct shot is represented for both examples (b, $Xmid = 50$ m, and d, $Xmid = 402$ m). Picked dispersion curves are represented for the fundamental (0), first (1), and second (2) higher modes, with error bars defined according to the workflow described in O'Neill (2003). Dispersion curves were limited down to the frequency ($f_{lim}$) where the spectral amplitude of the seismogram became too low. The corresponding maximum wavelength ($\lambda_{max}$) was also extracted to indicate typical investigation depth criterion.

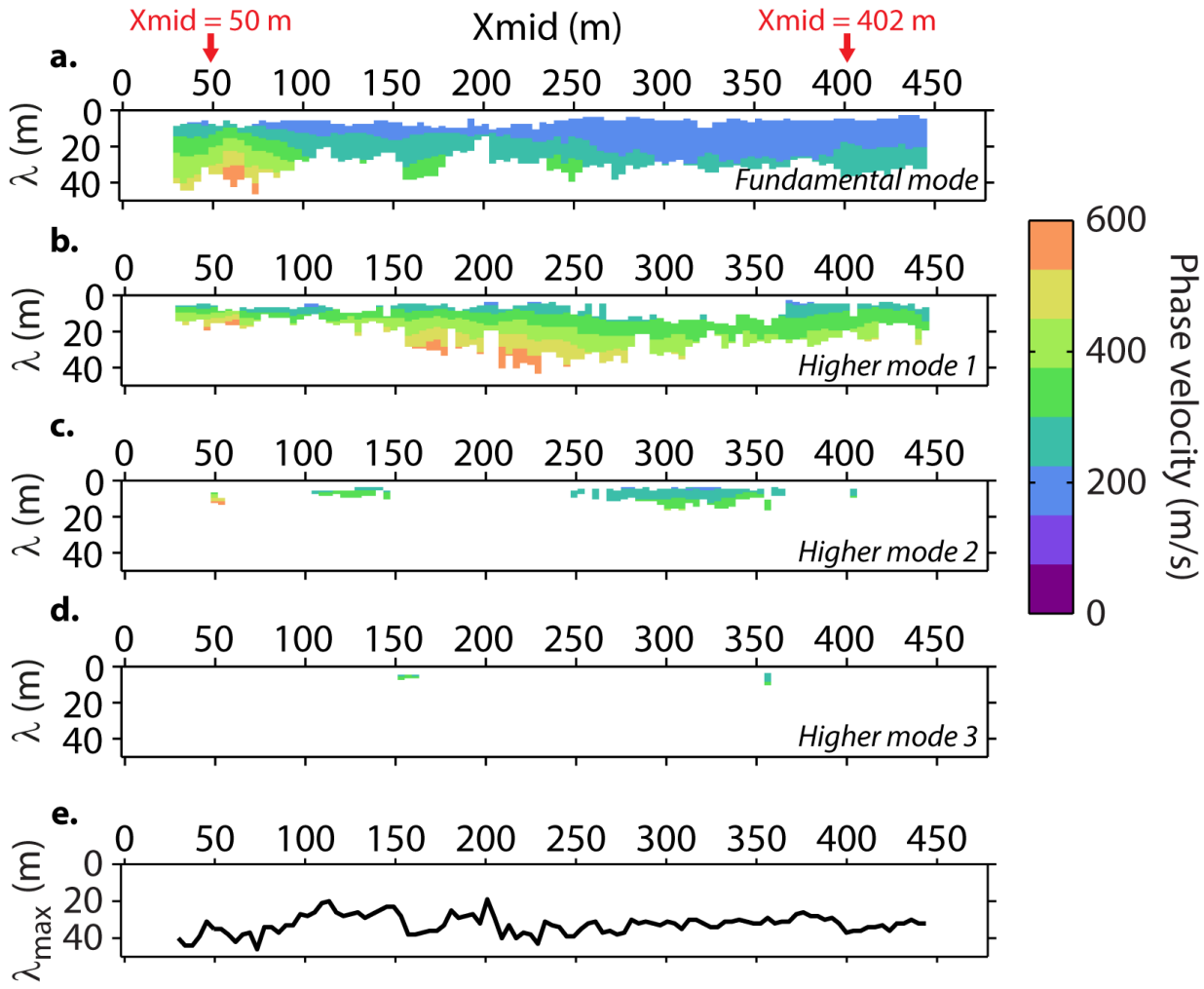


Figure 8: Pseudo-section of Rayleigh-wave phase velocity dispersion curves picked for the fundamental (a), first (b), second (c), and third (d) higher modes along the line after dispersion stacking, represented as a function of the wavelength ($\lambda$) and the spread mid-point ($Xmid$). (e) Maximum wavelength ($\lambda_{max}$) observed at each $Xmid$.

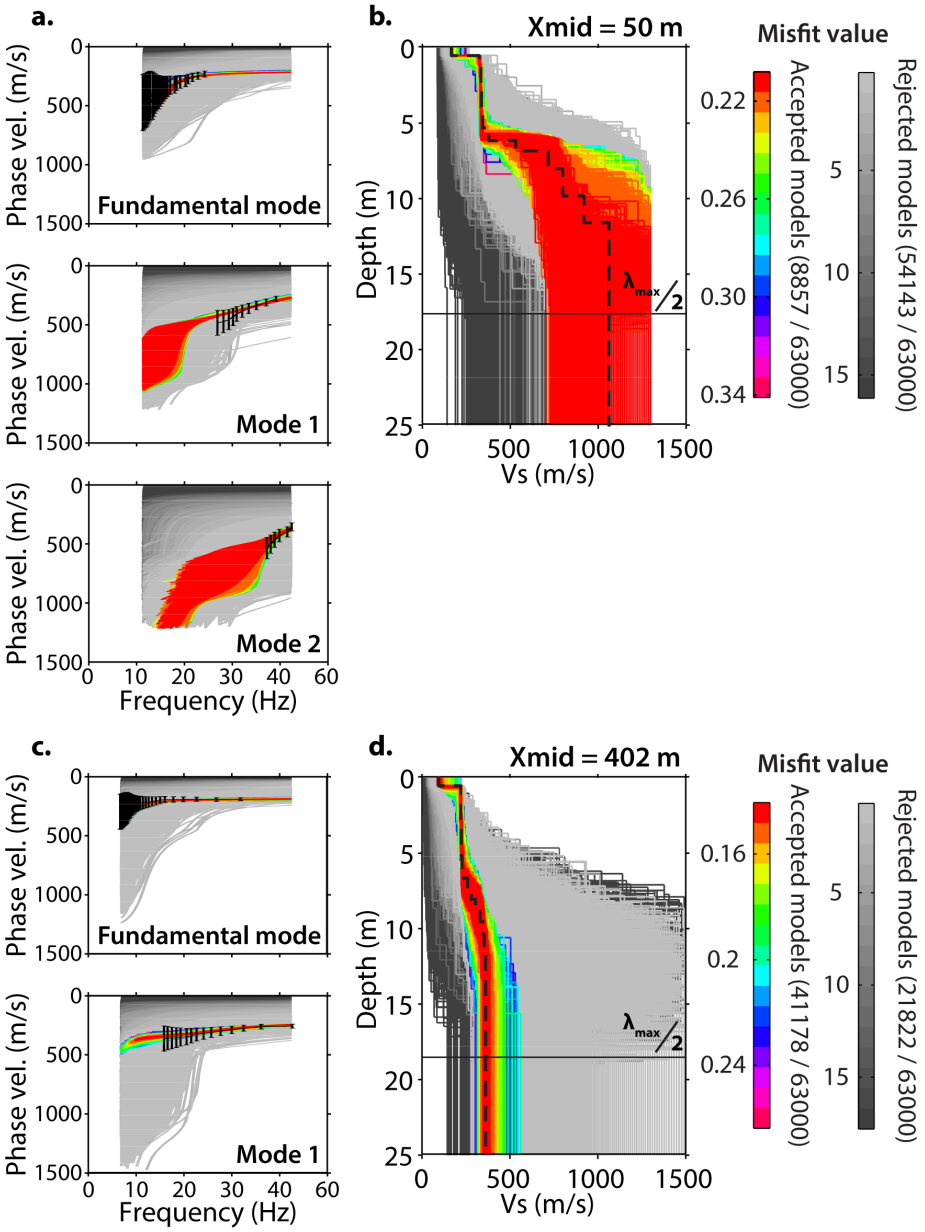


Figure 9: One-dimensional inversion of dispersion data (black error bars) extracted from the stacked dispersion image at $Xmid = 50$ m (a) and $Xmid = 402$ m (c) using the NA as implemented by Wathelet *et al.* (2004). Resulting models are represented for $Xmid = 50$ m (b) and $Xmid = 402$ m (d). Rejected models (i.e., at least one sample of the theoretical dispersion curves calculated from the model does not fit within the error bars) are represented according to their misfit with a greyscale, whereas accepted models (i.e., all samples of the theoretical dispersion curves calculated from the model fit within the error bars) are represented with a colour scale. Average parameters of all accepted models were used to build an average velocity structure associated with the centre of the extraction window (black dashed lines in b and d). The black solid line in (b) and (d) corresponds to $\lambda_{max}/2$ and indicates a typical investigation depth criterion.

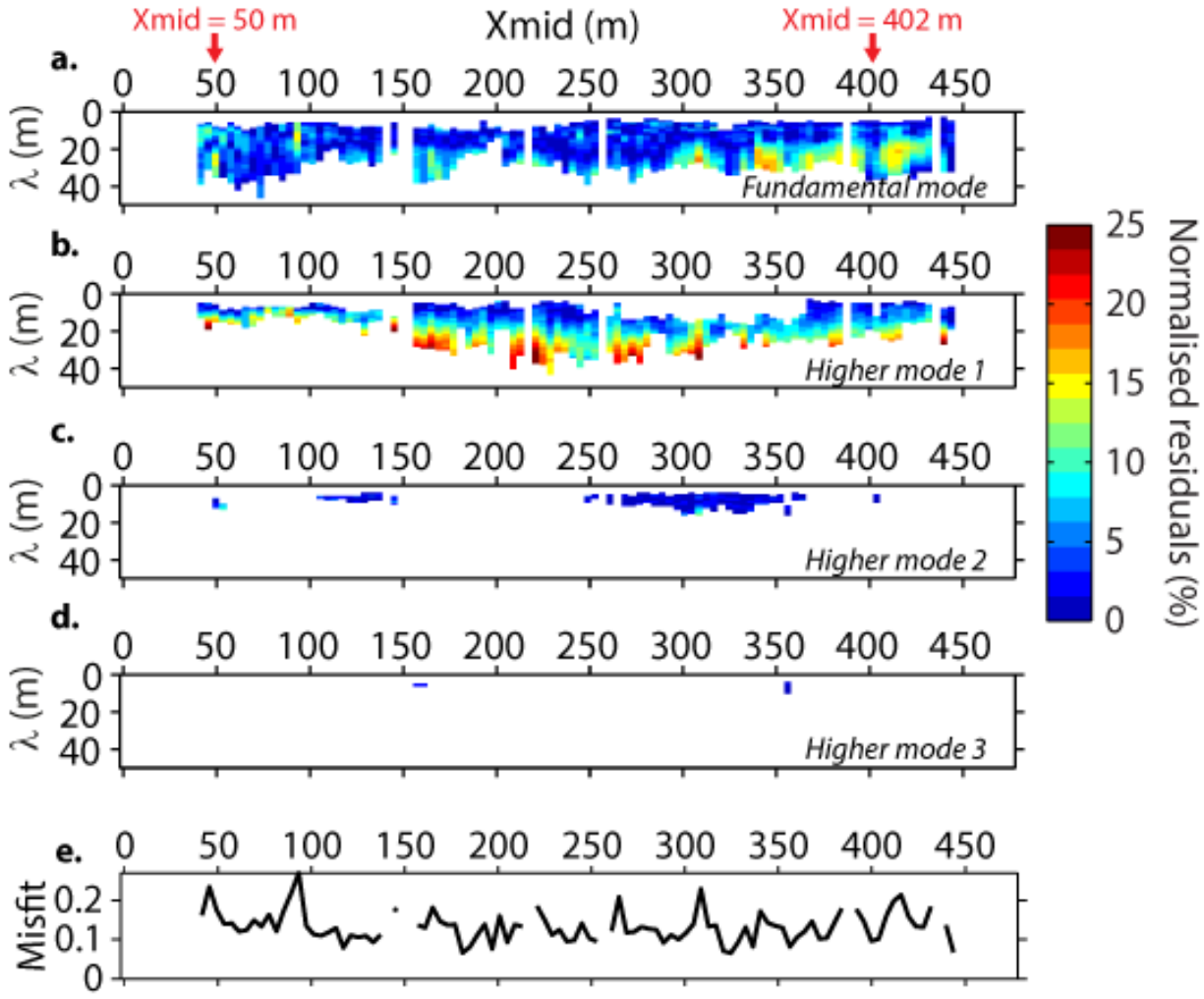


Figure 10: Pseudo-section of Rayleigh-wave phase velocity normalized residuals for the fundamental (a), first (b), second (c), and third (d) higher modes along the line after dispersion stacking. $\lambda$ is the wavelength. (e) Misfit values calculated with equation (1) for each 1D inversion along the line.

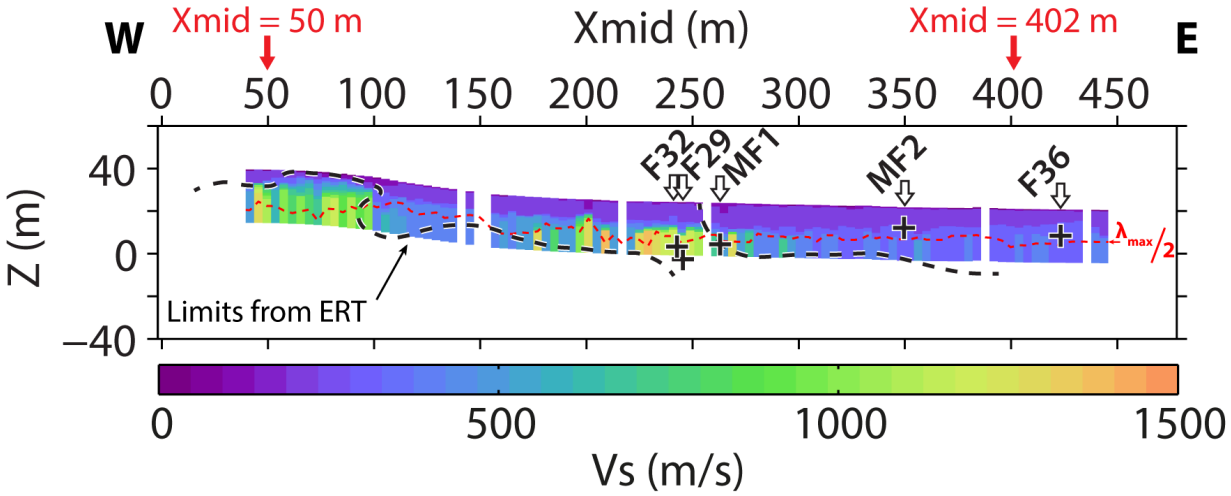


Figure 11: Pseudo-2D $V_S$ section constructed with all 1D $V_S$ models obtained from surface-wave profiling, overlaid with limits interpreted from ERT results. $\lambda_{max}/2$, represented with a black dashed line, corresponds to a typical investigation depth criterion. Positions of the nearest monitoring wells are projected along the WE line as in Fig. 2b.

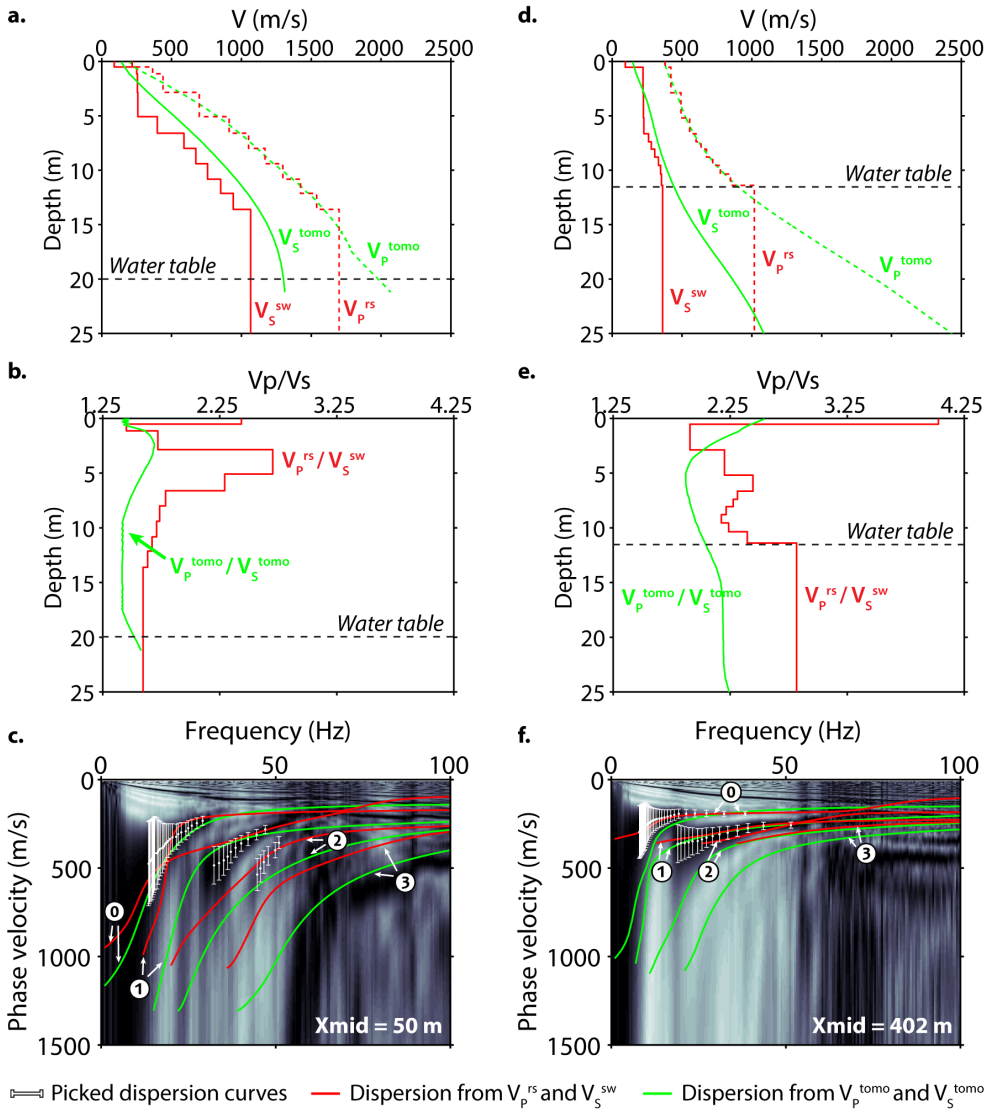


Figure 12: One-dimensional $V_S$ models obtained from SH-wave refraction interpretation ($V_S^{tomo}$, green solid line) and surface-wave dispersion inversion ($V_S^{sw}$, red solid line) at $Xmid$ = 50 m (a) and $Xmid$ = 402 m (d). One-dimensional $V_P$ models obtained from P-wave refraction tomography ($V_P^{tomo}$, green dashed line) and resampled to follow the layering of $V_S^{sw}$ ($V_P^{rs}$, red dashed line) are also represented in (a) and (d). One-dimensional $V_P/V_S$ models constructed from $V_S^{sw}$ and $V_P^{rs}$ ($V_P^{rs}/V_S^{sw}$, red solid line) and from $V_P^{tomo}$ and $V_S^{tomo}$ ($V_P^{tomo}/V_S^{tomo}$, green solid line) at $Xmid = 50$ m (b) and $Xmid = 402$ m (e). The water table level is represented with a black dashed line. In (a) and (b), the water table level is extrapolated from the nearest representative well implanted in the granite (around 100 m west from $Xmid = 50$ m). In (d) and (e), the water table level is interpolated from levels measured in wells MF2 and F36 (Fig. 2). Stacked dispersion image obtained at $Xmid = 50$ m (c) and $Xmid = 402$ m (f). The fundamental (0), the first (1), second (2), and third (3) higher modes' dispersion curves calculated from $V_S^{sw}$ and $V_P^{rs}$ (in red) and from $V_S^{tomo}$ and $V_P^{tomo}$ (in green) are superimposed on both images.

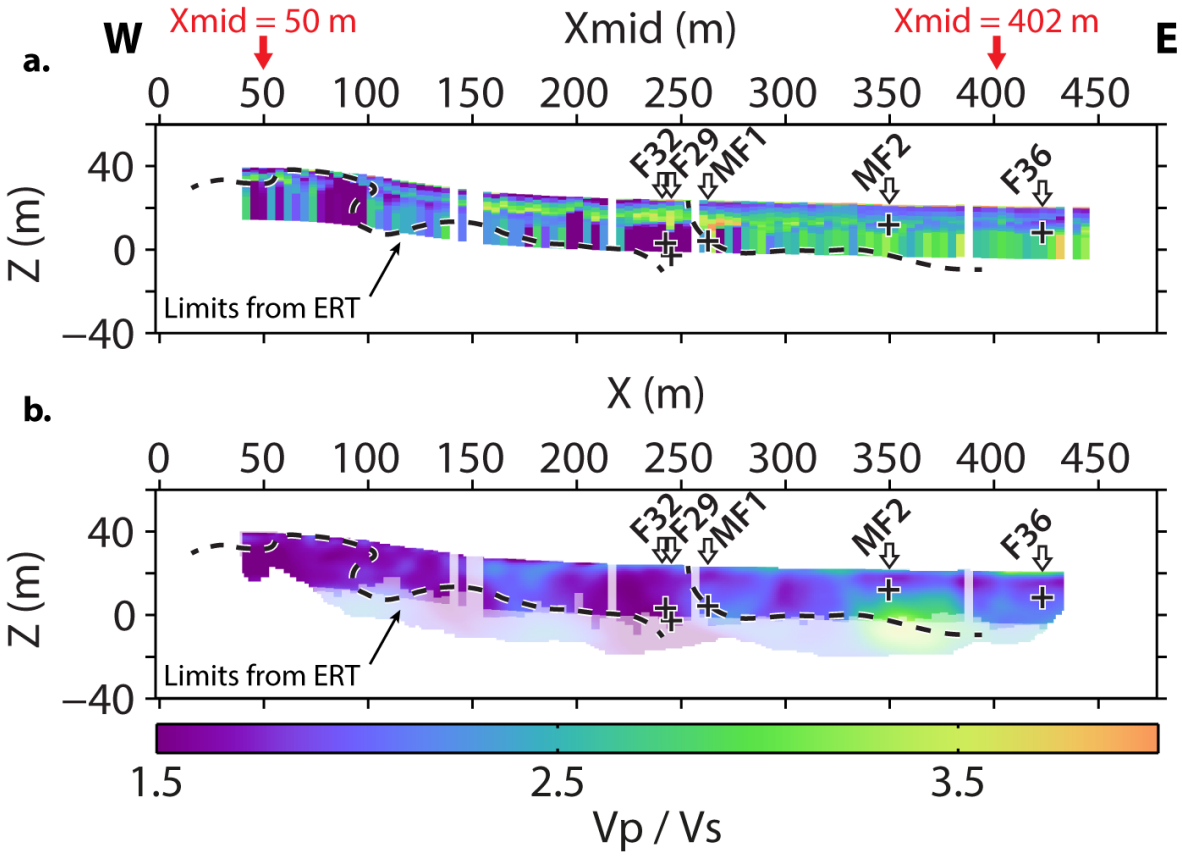


Figure 13: (a) Pseudo-2D $V_P/V_S$ section constructed with $V_S^{sw}$ obtained from surface-wave profiling and $V_P^{ts}$ obtained from P-wave tomography and resampled in depth according to the $V_S$ layering. (b) $V_P/V_S$ section computed from $V_P^{tomo}$ and $V_S^{tomo}$ models obtained from P- and SH-wave tomography. The shaded area in (b) corresponds to the extent of the $V_P/V_S$ pseudo-2D section in (a). Both sections are overlaid with limits interpreted from ERT results. Positions of the nearest monitoring wells are projected along the WE line as in Fig. 2b.